Editors' Suggestion

Selectivity of the KcsA potassium channel: Analysis and computation

Zilong Song and Xiulei Cao
Department of Mathematics and Statistics, York University, Toronto, Ontario, Canada M3J 1P3

Tzyy-Leng Horng
Department of Applied Mathematics, Feng Chia University, Taichung 40724, Taiwan
and National Center for Theoretical Sciences, Taipei Office, Taipei, Taiwan 10617

Huaxiong Huang*
Department of Mathematics and Statistics, York University, Toronto, Ontario, Canada M3J 1P3
and Fields Institute for Research in Mathematical Sciences, Toronto, Ontario, Canada M5T 3J1

(Received 26 February 2019; revised manuscript received 23 May 2019; published 7 August 2019)

Ion channels regulate the flux of ions through cell membranes and play significant roles in many physiological functions. Most of the existing literature focuses on computational approaches based on molecular dynamics simulation or numerical solution of the modified Poisson-Nernst-Planck (PNP) system. In this paper, we present an analytical and computational study of a mathematical model of the KcsA potassium channel, including the effects of ion size (Bikerman model) and solvation energy (Born model). Under equilibrium conditions, we obtain an analytical solution of our modified PNP system, which is used to explain selectivity of KcsA of various ions (K^+, Na^+, Cl^-, Ca^{2+}, and Ba^{2+}) due to negative permanent charges inside the filter region and the effect of ion sizes. Our results show that K^+ is always selected over Na^+, as smaller Na^+ ions have larger solvation energy. As the amount of negative charges in the filter exceeds a critical value, divalent ions (Ca^{2+} and Ba^{2+}) can enter the filter region and block the KcsA channel. For the nonequilibrium cases, due to difficulties associated with a pure analytical or numerical approach, we use a hybrid analytical-numerical method to solve the modified PNP system. Our predictions of selectivity of KcsA channels and saturation phenomenon of the current-voltage (I-V) curve agree with experimental observations.

DOI: 10.1103/PhysRevE.100.022406

I. INTRODUCTION

Rapid communication in many organisms relies on fast propagation of electric signals, which in turn depends on a specialized class of protein molecules called ion channels. When ion channels embedded in the cell membrane are opened by either chemical ligands or membrane depolarization, they allow ionic fluxes across the membrane and lead to rapid changes of membrane potentials. The dysfunction of ion channels causes a number of diseases. Specifically, potassium (K^+) channels regulate the flux of K^+ ions through cell membranes and participate in several physiological functions such as maintaining resting membrane potential, firing of nerve and muscle cells, secretion of hormones, and sensory transduction [1,2]. Therefore, understanding the underlying mechanisms that determine channel selectivity is of fundamental importance, for both biological and medical sciences [3–5].

K^+ channels are the most extensively studied family of ion channels, both experimentally and computationally, and the KcsA structure [6,7] has been the most popular one among K^+ channels since it is the first K^+ channel to be crystalized. Many computational and experimental data of KcsA are available for comparison. The x-ray crystallographic structures of distinct potassium channels reveal a common architecture of the pore [8,9]. Four subunits are symmetrically arranged around the channel axis, with each subunit having at least two transmembrane helixes separated by a reentrant P-loop and the selectivity filter (SF).

The SF of K^+ channels is the essential element to their permeation and selectivity mechanisms [10]. Tens to hundreds of millions (10^7–10^8) of K^+ ions per second can diffuse in single file down their electrochemical gradient across the membrane at physiological conditions [1,11–13]. Each subunit contributes to the SF with a conserved signature peptide, namely TVGYG in most of the channels [3]. The carbonyl oxygens of the backbone of the SF point toward the lumen and orchestrate the movements of ions in and out of the channel. These carbonyl oxygens together with the side-chain hydroxyl oxygen of a threonine residue define four ion-binding sites in the SF, designated S1–S4 starting at the extracellular side [14]. In addition, K^+ ion can bind in the central water-filled cavity of the pore and two alternate positions at the extracellular side of the pore [14].

The SF is generally too narrow to accommodate a K^+ ion with its hydration shell, and thus K^+ ions must be dehydrated to enter the SF, when attracted by the strong negative charges of carbonyl oxygens in the SF. A K^+ ion must replace its solvation shell by the carbonyl oxygens in the backbone of the SF. Each of these protein sites binds K^+ ions with a

*hhuang@fields.utoronto.ca

tight-fitting cage of eight carbonyl oxygen atoms that resembles the solvation shell of a hydrated K^+ ion.

The classical Poisson-Nernst-Planck (PNP) system has been widely applied to model ionic transport in biological setting as well as other areas [15–17]. Various analytical and computation studies of the PNP system can be found in the literature [18–20]. The current-voltage (I-V) relation is an important functional characteristic of ion channels and can be determined experimentally. PNP theory has been successfully applied to model wide ion channels, and has successfully reproduced experimentally observed I-V relation [21,22]. However, it is not suitable for narrow ion channels, such as KcsA. This is because classical PNP neglects the effect of ion sizes and therefore overestimates the K^+ ion occupancy of the SF. Also, classical PNP does not consider the solvation energy barrier that is encountered by ions entering the SF when dehydrated.

Various modified PNP system have been proposed to include steric or size effect of ions [23–29]. In this study, we choose the Bikerman model [30], which is one of the widely accepted models in the literature. The Bikerman model considers water as an additional species in the entropy, and it has been derived by using the mean-field theory in Ref. [31] to study a calcium channel. It has also been extended to include void as extra species in Refs. [29,32,33]. The Bikerman model with same ion sizes (called Borukhov model in Ref. [34]) has also been generalized to allow different ionic sizes in a modified PNP model in Ref. [34] by modifying the free energy. The Bikerman model is chosen because of its simplicity that allows us to obtain analytical results, which we believe can provide more physical insights into the mechanism of ion channels. In addition, solvation energy based on Born model [35–37] is included in the present formulation to capture the significant contribution in the free energy due to dehydration of ions.

It is well known that potassium channels have high selectivity of potassium ion over sodium ion (K^+ is 10^4 times more permeant than Na^+) [1]. Though K^+ and Na^+ have the same valence and therefore have the same electrostatic affinity to carbonyl oxygens in the SF, K^+ encounters less Born solvation energy barrier than Na^+ due to its slightly larger size compared with Na^+. However, few studies have been conducted on the selectivity between K^+ and alkaline earth ions like Ca^{2+} and Ba^{2+}. Alkaline earth ions generally have stronger electrostatic affinity to the SF than K^+ due to their double charge, but at the same time also bear larger Born solvation energy barrier again due to their double charge. The blockage of KcsA by Ba^{2+} has demonstrated this strong competition of the SF occupancy between electrostatic affinity and solvation energy [38].

In the literature, selectivity of ion channels is defined in various ways by specific experiments or specific models, see Ref. [39] for a review. On the basis of thermodynamic binding equilibrium, selectivity is often defined as the free-energy difference of different ions from the chamber to a binding site in the filter [9,40], which is widely used in MD simulations. Classically, in nonequilibrium setting or in experimental measurements, selectivity is sometimes defined as the ratio of currents (or permeability in GHK model) of different ions through the channel [41,42], characterized by I-V relations or conductance-concentration relations. In the equilibrium case, Liu *et al.* [43] adopted a Poisson-Fermi model with nonlocal electrostatics, and computed the free energy differences for selectivity of Na^+ and K^+, which agrees with MD results. In the nonequilibrium case, the selectivity of gramicidin A channel and a calcium channel was investigated in Ref. [44] based on the PNP-Fermi model, showing agreement with experimental I-V data. With the present continuum (modified PNP) model, selectivity in this paper is defined as the ratio of concentrations of different ions in the filter region [45–50], under normal physiological conditions in the chamber. This is slightly different from those based on discrete models or MD simulations, but it bears some similarities in causes and consequences. In the equilibrium case, we can also compute free-energy differences as in MD simulations [40]. In the nonequilibrium case, one consequence of this definition of selectivity is that only selected ions can go through the channel, and the results of their currents can be directly compared with experimental I-V data [13].

Here we employ a one-dimensional modified PNP model to analytically and numerically study the mechanisms of (i) channel selectivity among K^+ and other ions; and (ii) level off of current I when voltage V increases, known as saturation in the literature [13,51–53]. More precisely, we provide analytical formulas that can be used to explain selectivity among K^+, Na^+, Cl^-, Ca^{2+}, and Ba^{2+}. Selectivity is mainly influenced by permanent negative charges in the SF and solvation energies associated with the ion sizes and valences. The smaller ion size of Na^+ compared with K^+ gives a larger solvation energy barrier to enter the filter, and hence its concentration is exponentially smaller (not selected). When negative charge in the SF exceeds a critical value (given by the ion size of K^+), divalent cations coexist with K^+ by squeezing some K^+ out of the SF, since divalent cations can do a better job in balancing the strong negative charges in the narrow SF. Although Born solvation energy is increased by this recruitment of divalent cations into the SF, it is compensated by a greater reduction of the electrostatic energy. As the result, the total energy is lower. We have studied the I-V curves by analytical, numerical, and hybrid methods, and our results are in agreement with experimental observations. Our solutions have revealed that the main reason for saturation of the I-V curve is that the concentrations of selected ions approach 0 in the chamber at the edge of filter when the voltage becomes large. Positivity of concentration sets an upper limit for the flux or current, known as saturation.

The manuscript is arranged as follows. Section II formulates the mathematical model, i.e., modified PNP system consisting of the Bikerman and Born models. Section III focuses on the equilibrium case with zero flux and addresses the issues of selectivity. Section IV provides analytical results for the nonequilibrium case and discusses the I-V curve. Numerical simulations are conducted in Sec. V and a hybrid analytical-numerical analysis is given in Sec. VI. Finally, some concluding remarks are provided in Sec. VII.

II. MATHEMATICAL MODEL

We consider the Bikerman model with specific ion sizes [30] and include permanent charge and solvation energy into

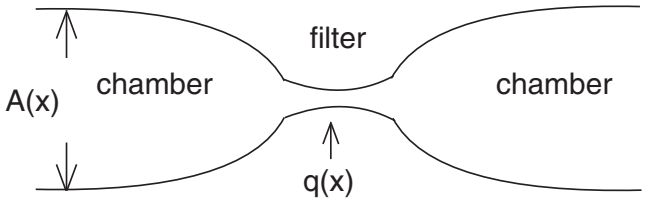

FIG. 1. Sketch of the potassium KcsA channel.

the Poisson-Nernst-Planck (PNP) formulation. The original one-dimensional (1D) system for $-L < x < L$ is

$$\begin{aligned} &-\frac{1}{A(x)}\partial_x(\epsilon_0\epsilon_r(x)A(x)\partial_x\phi) = e_0\left(\sum_{k=1}^{n} z_k c_k - q(x)\right), \\ &\partial_t c_i + \frac{1}{A(x)}\partial_x J_i = 0, \\ &J_i = -A(x)\frac{D_i}{k_B T}c_i\partial_x\mu_i, \end{aligned} \tag{1}$$

where c_i $(i = 1, .., n)$ denote the concentrations of ions, ϕ is the electric potential, $A(x)$ is the cross sectional area, $q(x)$ is the permanent charge (positive q means negative fixed charge), $\epsilon_r(x)$ is the relative permittivity, and k_B, T, ϵ_0, e_0 are some constants (see Appendix A). The electrochemical potentials are given by

$$\begin{aligned} \mu_i = k_B T\left[\log\left(c_i a_i^3\right) - \log\left(1 - \sum_{k=1}^{n} c_k a_k^3\right)\right] \\ + z_i e\phi + W_i, \quad i = 1, .., n, \end{aligned} \tag{2}$$

where a_i are the effective ion diameters, and W_i is the solvation energy [36,37]

$$W_i(x) = \frac{z_i^2 e_0^2}{4\pi\epsilon_0 a_i}\left(\frac{1}{\epsilon_r(x)} - 1\right). \tag{3}$$

The form of μ_i without the solvation energy was derived by the mean-field theory in Ref. [31] and later reviewed in Ref. [30]. This modified PNP system can be derived from the free energy in Appendix C with certain approximation [30].

Figure 1 schematically shows the setup, where the filter of the channel lies between two chambers, linking extracellular and intracellular spaces, respectively. The length of the filter is L_f and the length of each chamber is set as L_b (then reference length is $L = L_b + \frac{1}{2}L_f$), where some part of reservoir is included if we consider a relatively large L_b. The cross sectional area $A(x)$ in the filter is much smaller than that of the chamber region. The permanent negative charge $q(x)$ due to carbonyl oxygens and threonine residues is confined in the small volume of the filter, so the effective $q(x)$ in the model is extremely large compared with the chamber concentrations of ions [54,55]. This further implies that the filter attracts counter-ions and thus the saturation of ions in the filter means few water molecules in the filter or ions are dehydrated. Therefore, the dielectric constant $\epsilon_r(x)$ would be much smaller in the filter, and this justifies the introduction of the above solvation energy $W_i(x)$, which gives the energy barrier from the chamber to the filter. In later analysis, the solvation energy also causes jumps in concentrations from the chamber to the filter while maintaining continuous electrochemical potentials μ_i.

In the chamber, the model is approximately the classic PNP system, where the size effect is negligible and $q(x) = 0$. With this in mind, we do a traditional nondimensionalization with reference scales in the chamber. We set

$$\begin{aligned} &\tilde{x} = \frac{x}{L}, \quad \tilde{c}_i = \frac{c_i}{c_0}, \quad \tilde{\phi} = \frac{\phi}{\phi_0}, \quad \tilde{D}_i = \frac{D_i}{D_0}, \\ &\tilde{t} = \frac{t}{L^2/D_0}, \quad \tilde{\epsilon}_r = \frac{\epsilon_r}{\epsilon_{rb}}, \quad \tilde{a}_i = \frac{a_i}{a_0}, \quad \tilde{A} = \frac{A}{A_b}, \\ &\tilde{L}_f = \frac{L_f}{L}, \quad \tilde{q} = \frac{q}{c_0}, \quad \tilde{W}_i = \frac{W_i}{k_B T}, \end{aligned} \tag{4}$$

where a_0 is a reference ion diameter, D_0 is a reference diffusion constant, A_b is a reference cross sectional area in the chamber and ϵ_{rb} is the (maximum) relative permittivity at the far end of the chamber (see Eq. (A2) in Appendix A for their values).

By removing the tilde, the dimensionless system in $-1 < x < 1$ is

$$\begin{aligned} &-\epsilon^2\frac{1}{A(x)}\partial_x(\epsilon_r(x)A(x)\partial_x\phi) = \sum_{k=1}^{n} z_k c_k - q(x), \\ &\partial_t c_i + \frac{1}{A(x)}\partial_x J_i = 0, \\ &J_i = -A(x)D_i c_i\partial_x\mu_i, \end{aligned} \tag{5}$$

where $i = 1, ..., n$ and

$$\begin{aligned} \mu_i(x) = \log[c_i(x)] - \log\left(1 - \sum_{k=1}^{n} c_k(x)a_k^3\delta\right) \\ + z_i\phi(x) + W_i(x), \\ W_i(x) = \frac{z_i^2}{a_i}\left(\frac{1}{\epsilon_{rb}\epsilon_r(x)} - 1\right)W_0, \end{aligned} \tag{6}$$

where the first term in μ_i is originally $\log(c_i a_i^3\delta)$ after nondimensionalization, but we removed the constant $\log(a_i^3\delta)$ from μ_i since this will not affect the system. The dimensionless parameters are

$$\epsilon = \sqrt{\frac{\epsilon_0\epsilon_{rb}k_B T}{e_0^2 c_0 L^2}}, \quad \delta = a_0^3 c_0, \quad W_0 = \frac{e_0^2}{4\pi\epsilon_0 a_0 k_B T}. \tag{7}$$

Please refer to Appendix A for the estimates of parameters in this system, and note that $\delta \ll 1$. Since the classical PNP formulation is a model for dilute solutions [26,56], it can be recovered when $\epsilon_r(x)$ is constant and the concentrations c_i $(i = 1, .., n)$ are $O(1)$ (i.e., dilute solution $c_i \ll 1/\delta$) as in the chamber region. When ϵ_r is constant, W_i is constant for each ion, and hence can be removed from μ_i in Eq. (6) (since differentiation gives 0). When c_k is $O(1)$ as in the chamber region, since $\delta \sim 10^{-3}$ is a small parameter and $a_k \sim O(1)$, $c_k a_k^3\delta$ in the second term of μ_i in Eq. (6) can be neglected. Therefore, it reduces to the classical PNP as first approximation in terms of δ for the chamber region. However, in the filter region, c_k is large (of order $1/\delta$), and $c_k a_k^3\delta$ cannot be neglected. Moreover the variation in ϵ_r gives the solvation energy barrier from the chamber to the filter.

III. EQUILIBRIUM CASE WITH ZERO FLUX

In this section, we study the selectivity of the channel in the equilibrium case, for simplicity. We will see the conclusions also hold for the nonequilibrium case with finite fluxes. This is reflected in the analysis of this section that the boundary conditions (inducing finite flux when different) have a negligible or exponentially small impact on the results. This is also verified by analytical and numerical results in the nonequilibrium case, as the selected ions have almost constant electrochemical potential μ_i in the filter (like the equilibrium case), see figures of μ_i in Secs. IV and V and analysis before Eq. (67). The equilibrium case in this section is related to the equilibrium binding in experiments or MD simulations.

The same boundary conditions at the two ends of the chamber are used

$$c_i(x) = c_{ib}, \quad \phi(x) = \phi_b, \quad \text{at} \quad x = \pm 1, \tag{8}$$

where $i = 1, .., n$ and the electro-neutrality condition $\sum_{i=1}^{n} z_i c_{ib} = 0$ is satisfied. Therefore, there is no flux across the filter. The aim is to study the relative concentrations of ions in the filter under different situations, which would imply the selectivity.

In the general case, we notice that by definition of μ_i in Eq. (6) we can solve c_i ($i = 1, .., n$) in terms of ϕ and μ_i (see Appendix B and Ref. [57]):

$$c_i = \frac{e^{\mu_i - W_i - z_i\phi}}{(1 + F\delta)}, \quad F = \sum_{k=1}^{n} a_k^3 e^{\mu_k - W_k - z_k\phi}. \tag{9}$$

For the equilibrium case, by $J_i = 0$, we conclude that μ_i is constant throughout the filter and the chamber

$$\mu_i(x) = B_i = \log(c_{ib}) - \log\left(1 - \sum_{k=1}^{n} c_{ib} a_k^3 \delta\right) + z_i\phi_b + W_i(1), \tag{10}$$

where the constant B_i is determined by the boundary conditions in Eq. (8). In this case, by substituting Eq. (10) into (9), c_i is expressed explicitly in terms of ϕ. When c_i is $O(1)$ as in the chamber region, Eq. (9) reduces to the classical Boltzmann distribution at leading order (i.e., δ tends to 0),

$$c_i = e^{\mu_i^b - z_i\phi}[1 + O(\delta)], \quad \mu_i^b = \log(c_{ib}) + z_i\phi_b, \tag{11}$$

where the W_i term has canceled with that in μ_i.

Since the filter region is quite small, it is natural to adopt an effective charge [55,58]. We assume $q(x) = q$ is a large constant in the filter, and treat q as a crucial parameter. Depending on the relative magnitude of q, we have either the electroneutral (EN) case or the non-EN case in the filter. We also assume $\epsilon_r(x) = \epsilon_{r0}$ in the filter, where ϵ_{r0} is constant (i.e., 1/40, corresponding to original $\epsilon_r = 2$). Note by the choice of scaling in Eq. (4), we have $\epsilon_r(\pm 1) = 1$.

A. K^+/Na^+ selectivity

In this subsection, we consider the case with three ions K^+, Na^+, and Cl^- (respectively, c_1, c_2, and c_3), and study the selectivity between Na^+ and K^+.

From the expressions of c_1 and c_2 in Eqs. (9) and (10), we get in the filter

$$\frac{c_1}{c_2} = \frac{e^{B_1 - W_1(0)}}{e^{B_2 - W_2(0)}}. \tag{12}$$

Thus, the ratio c_1/c_2 is a constant independent of ϕ and x in the filter. More precisely, we have

$$B_i - W_i(0) \approx -\Delta W_i + \log c_{ib} + z_i\phi_b, \quad i = 1, ..., n, \tag{13}$$

where the $O(\delta)$ term in the chamber has been dropped and ΔW_i is the barrier from the chamber to the filter due to the solvation energy:

$$\Delta W_i = W_i(0) - W_i(1) = \frac{z_i^2}{a_i}\left(\frac{1}{\epsilon_{rb}\epsilon_{r0}} - \frac{1}{\epsilon_{rb}}\right)W_0, \quad i = 1, ..., n. \tag{14}$$

Since the ion diameter of K^+ is larger than that of Na^+, the barrier of K^+ from the chamber to the filter is smaller, i.e.,

$$a_1 > a_2 \Rightarrow \Delta W_1 < \Delta W_2. \tag{15}$$

From the data in Eq. (A3) of Appendix A, we get $\Delta W_i \sim W_0 \sim O(10^2)$, thus the term ΔW_i dominates the ratio Eq. (12), and hence c_2 is always exponentially smaller than c_1. As both c_1 and c_2 are at most of the order $O(q)$, the concentration c_2 is exponentially small and negligible in the filter. This means that K^+ is favored or selected in the filter compared with Na^+, and this fact is independent of q. Based on data in Eqs. (A2) and (A3) of Appendix A, we get

$$\Delta W_1 = 98.4, \quad \Delta W_2 = 133.1. \tag{16}$$

This implies that the term ΔW_i dominates in Eqs. (12) and (13), unless the chamber contraction c_{2b} is 10^{15} times larger than c_{1b}. Under normal physiological conditions [i.e., $c_{ib}, \phi_b \sim O(1)$] in the chamber, we obtain the selectivity of K^+ over Na^+ through the ratio

$$\frac{c_1}{c_2} \sim 10^{15}. \tag{17}$$

Since the boundary values ϕ_b, c_{ib} ($i = 1, 2, 3$) have negligible effect (ϕ_b has no effect here), one can imagine this conclusion holds for the nonequilibrium case. One can rigorously prove it by noting μ_i is monotone in the nonequilibrium case with finite flux.

1. EN case

From the data in Eqs. (A3) and (A4) of Appendix A, we obtain $q \sim O(1/\delta)$. We have EN case when q does not exceed the critical value:

$$q < \frac{1}{a_1^3\delta}. \tag{18}$$

Since there is limited space in the filter, physically the critical value on the right-hand side is the maximum effective charge that ions of K^+ can provide to balance the negative permanent charge q when the filter is fully filled with K^+. In this case, K^+ and its size a_1 are crucial because of the selectivity in Eq. (17). In the case of Eq. (18), the same amount of K^+ will be recruited into the filter to balance the negative permanent charge q, leading to EN and constant ϕ in most part of filter.

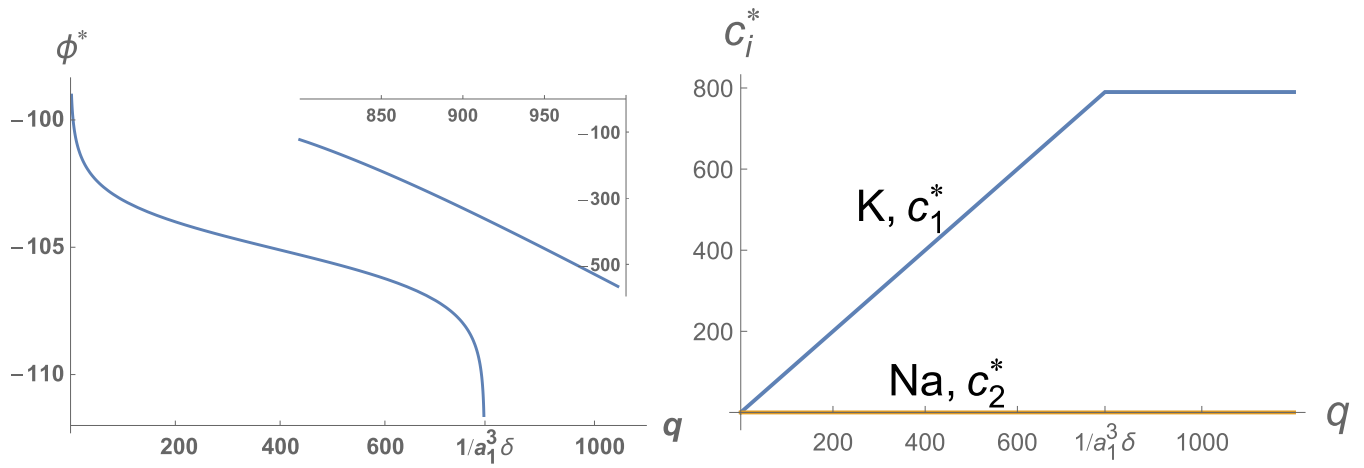

FIG. 2. Dependence of ϕ^* and c_i^* $(i = 1, 2)$ in the filter on permanent charge q.

When q exceeds that critical value, even the maximum amount $1/a_1^3\delta$ of K^+ can not balance q. It is no longer EN in filter (see Sec. III A 2), and the extra charge $q - 1/a_1^3\delta$ will be balanced by the change of electric field (i.e., left-hand side of Eq. (5)), and therefore the profile of ϕ behaves like a quadratic function instead of a constant.

Here, the EN condition in the filter,

$$c_1 + c_2 - c_3 = q, \tag{19}$$

provides a nonlinear equation for ϕ, with the help of Eqs. (9) and (10). In fact, this is a quadratic equation for e^{ϕ}. The analytic solution involves many exponentially large and exponentially small terms, and can easily lead to wrong or complex solutions by direct computation with softwares (e.g., Mathematica). It is easy to prove that c_3 is also exponentially small. As a leading order approximation, we have

$$c_1^* = q, \quad c_k^* = 0, \quad k = 2, 3,$$
$$\phi^* = -\Delta W_1 + \log c_{1b} + \phi_b + \log\left(1 - a_1^3 q\delta\right) - \log q, \tag{20}$$

which can also be obtained directly from the analytical solution by keeping the essential exponentially small terms and dropping the high-order exponentially small terms.

Remark. In the above analysis, by EN condition we mean that it is valid in the majority middle part of the filter region. Actually, near the two edges of the filter (or interface of the filter and the chamber), denoted as $x = \pm s$, there is a tiny boundary layer (BL) due to large q and small ϵ_r in Eq. $(5)_1$, where the variation of ϕ is quite large. In the approximation Eq. (20), only some exponentially small terms are dropped, so the expressions are accurate enough.

Figure 2 shows the dependence of the above solution on q, with $c_{1b} = 1$, $\phi_b = 0$ and data in Eq. (A3) of Appendix A. The value of c_{2b} [assumed as $O(1)$], the profiles of $A(x)$ and $\epsilon_r(x)$, provided $\epsilon_r(0) = 1/40$, will not affect the above approximation in the filter. This will be verified in numerical simulations. Based on selected values of the parameters, the critical value is $q = 1/a_1^3\delta \approx 790$ in Fig. 2. When q is near 0 or near this critical value, the above solution is not valid, as indicated by two singularities in Fig. 2(a). When q exceeds the critical value, one should solve the full Eq. $(5)_1$ in the filter instead of the EN condition, as we see in the next subsection. For $q > 1/a_1^3\delta$, the subfigure in Fig. 2(a) (the minimum of ϕ) and the curve in Fig. 2(b) are based on the next subsection. Figure 2(b) shows the selectivity of K^+ and Na^+ in the filter.

2. Non-EN case

For this case, we can not use the EN condition and instead we should solve the full Eq. (5). Since the length of the filter is at the same scale as the BL in the classical PNP of the chamber region, we introduce a new scale $X = x/\epsilon$ to study the system. For the equilibrium case, the equation for ϕ is

$$-\frac{1}{A(X)}[\epsilon_r(X)A(X)\phi'(X)]' = \sum_{k=1}^{n} z_k c_k - q(X), \quad -\infty < X < \infty, \tag{21}$$

where prime denotes the derivative with respect to X. In the above, we consider a relatively long chamber region, so the infinite domain is used as an approximation (this causes essentially no difference). The position of the interface between the filter and the chamber is $X = S \equiv L_f/2\epsilon$, where $S \sim O(1)$.

For simplicity, we consider a simple geometry (see Fig. 3) where the cross-sectional area $A(X)$, the fixed charge $q(X)$, and the relative permittivity $\epsilon_r(X)$ are constants in either the

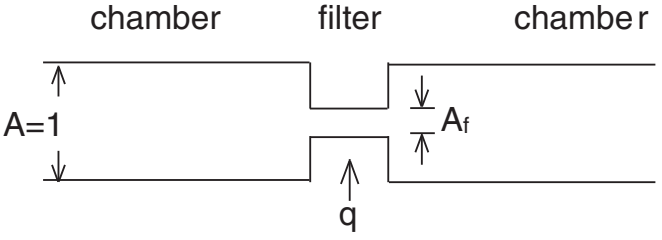

FIG. 3. Sketch of the potassium channel with simplified geometry.

chamber or the filter region. We denote

$$A(X) = A_f, \quad \epsilon_r(X) = \epsilon_{r0}, \quad q(X) = q, \quad -S < X < S,$$
$$A(X) = 1, \quad \epsilon_r(X) = 1, \quad q(X) = 0, \quad |X| > S. \tag{22}$$

Note that some typical values are

$$A_f = 1/30, \quad q = 10^3, \quad \epsilon_{r0} = 1/40. \tag{23}$$

Due to symmetry, we consider only the interval $X \in [0, \infty)$. For the chamber region, Eq. (21) reduces to the classical Poisson-Boltzmann equation by neglecting the $O(\delta)$ term,

$$-\phi''(X) = e^{-\phi} - e^{\phi}, \quad S < X < \infty, \tag{24}$$

where we have assumed the boundary conditions at ∞,

$$\phi(\infty) = 0, \quad c_1(\infty) + c_2(\infty) = c_3(\infty) = 1. \tag{25}$$

It is easy to get

$$\phi' = \sqrt{2}(e^{-\phi/2} - e^{\phi/2}), \quad S < X < \infty, \tag{26}$$

and hence obtain the solution $\phi(X)$ in the chamber region (see Eq. (B4) in Appendix B).

In the filter, we have from Eq. (21) and the symmetry condition that

$$-\epsilon_{r0}\phi''(X) = c_1 + c_2 - c_3 - q, \quad 0 < X < S,$$
$$\phi'(0) = 0, \quad \text{at} \quad X = 0, \tag{27}$$

where c_i $(i = 1, 2, 3)$ are given by Eqs. (9) and (10). One can easily prove that the function $\phi(X)$ is monotonically increasing throughout the interval $[0, \infty)$, since $c_2 + c_1 < q$ in the filter. For the filter region, since c_2 is exponentially small [see the analysis below Eq. (12)], it can be neglected. In addition, by the expression of c_3 in Eqs. (9) and (10) and data in Eq. (A3) of Appendix A, we obtain

$$c_3 < e^{B_3 - W_3(0) + \phi}, \quad B_3 - W_3(0) \approx -\Delta W_3 \approx -75. \tag{28}$$

From the fact that ϕ is increasing, we get that $\phi < 0$, thus c_3 is always exponentially small and can be neglected. Therefore, the filter Eq. $(27)_1$ is simplified to

$$-\epsilon_{r0}\phi''(X) = c_1 - q, \quad c_1 = \frac{e^{B_1 - W_1(0) - \phi}}{1 + \delta a_1^3 e^{B_1 - W_1(0) - \phi}}. \tag{29}$$

By integration, we get

$$\sqrt{\epsilon_{r0}}\phi' = \sqrt{2[G(\phi) - G(\phi_0)]},$$
$$X = \sqrt{\frac{\epsilon_{r0}}{2}} \int_{\phi_0}^{\phi} \frac{1}{\sqrt{G(\phi) - G(\phi_0)}} d\phi, \tag{30}$$

where $\phi_0 \equiv \phi(0)$ is to be determined, and the function $G(\phi)$ is given by

$$G(\phi) = \int^{\phi} q - c_1 d\phi = q\phi + \frac{1}{a_1^3\delta} \log\left(1 + a_1^3\delta e^{B_1 - W_1(0) - \phi}\right). \tag{31}$$

At interface $X = S$, we have

$$\phi(S-) = \phi(S+), \quad \epsilon_{r0} A_f \phi'(S-) = \phi'(S+). \tag{32}$$

Denote $\phi(S\pm) = \phi_s$, then the two quantities ϕ_0 and ϕ_s are determined by

$$A_f \sqrt{\epsilon_{r0}(G(\phi_s) - G(\phi_0))} = e^{-\phi_s/2} - e^{\phi_s/2},$$
$$\sqrt{\frac{\epsilon_{r0}}{2}} \int_{\phi_0}^{\phi_s} \frac{1}{\sqrt{G(\phi) - G(\phi_0)}} d\phi = S. \tag{33}$$

Once they are found, we get the explicit solutions for the filter and the chamber regions.

Figure 4 shows the profiles of $\phi(X)$ and $c_1(X)$, with values in Eqs. (23) and (A3) and $c_1(\infty) = 1$. In the filter region, Figure 4(a) shows that the minimum value of ϕ is much smaller than the EN case, and Fig. 4(b) shows that $\phi \sim O(1)$ in the chamber region. Figure 4(c) shows the profile of c_1 in the right-half filter region, indicating that $c_1 = 1/a_1^3\delta$ in the majority middle part of the filter and there is an inner transition from exponentially small value to that critical value. This means that in most part of the filter, it is fully packed

$$1 - \delta \sum_{i=1}^{3} a_i^3 c_i = 0, \tag{34}$$

but it still needs the derivatives $\phi''(X)$ to balance the large q. The solutions (e.g., minimum ϕ_0 and interface value ϕ_s) are mainly influenced by dimensionless quantities L_f (position S), A_f and ϵ_r in the filter.

Remark. In Sec. III A 1, we considered only the constant solution $\phi = \phi^*$ in the middle part of the filter. Actually, the constant ϕ^* is connected to the chamber by a standard BL in the filter and near the two edges. The solution in the filter can be easily constructed in a way similar to the above analysis, and is given as

$$X = S + \sqrt{\frac{\epsilon_{r0}}{2}} \int_{\phi_s}^{\phi} \frac{1}{\sqrt{G(\phi) - G(\phi^*)}} d\phi, \quad 0 < X < S, \tag{35}$$

where ϕ_s determined by Eq. $(33)_1$ with $\phi_0 = \phi^*$ there. The results for ϕ and c_1 are shown in Fig. 5 for the case $q = 600 < 1/a_1^3\delta$ with other parameters as before. One can clearly see the typical BLs of ϕ near the two edges in the filter.

The high selectivity of the SF for larger K^+ over smaller Na^+ has been also intensively studied by molecular dynamics (MD) [13,59–61] and experiments [62,63], just to name a few. Experiments show Na^+ can block KcsA K^+ current from intracellular side but not from extracellular side [62]. This observation is explained by MD studies that Na^+ would encounter a much larger energy barrier than K^+ when approaching S2 binding site in multi-cation knock-on entering the SF from extracellular side [59], and all binding sites are more selective to K^+ than Na^+ except the internal water cavity site lying at the entrance of the SF from intracellular side [60]. Based on analysis and solutions in this section, we can calculate the difference in free energies for K^+ and Na^+, given in Appendix C. With $q = 950$, the total free energy difference is

$$\Delta\Delta\mathcal{F}(K^+ \to Na^+) = 6.2\,\text{kcal/mol}, \tag{36}$$

which is consistent with the MD estimate 5–6 kcal/mol. The electrostatic energy and solvation energy are the two main parts of the energy difference. The solvation energy difference

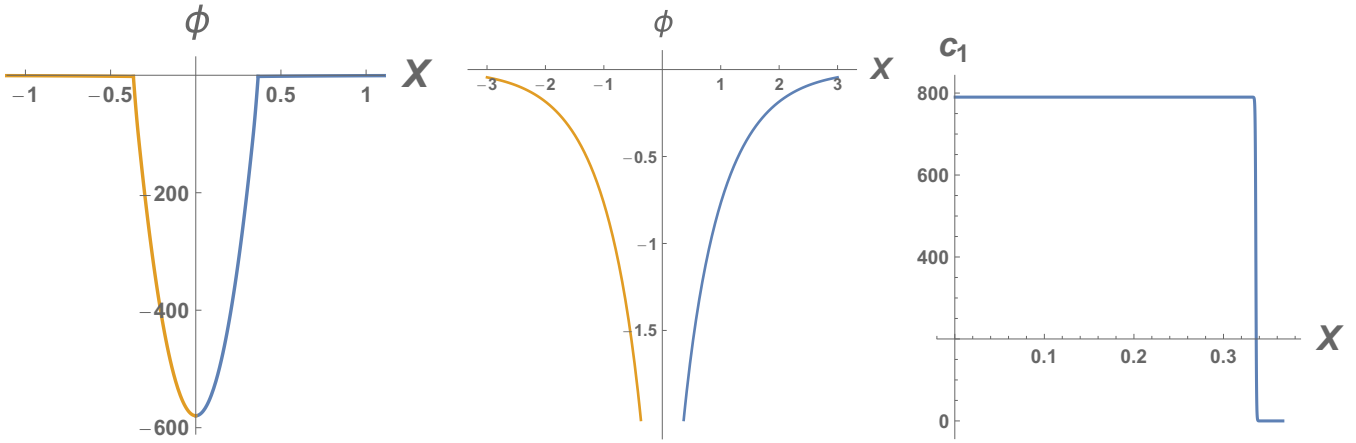

(a) (b) (c)

FIG. 4. The profiles for the case $q = 1000 > 1/a_1^3\delta$: (a) ϕ in both filter and chamber, (b) ϕ in the chamber, (c) c_1 in the right-half interval of the filter.

is $\Delta\Delta\mathcal{F}_w = 20.8\,\text{kcal/mol}$, which means K^+ is favored due to its larger size. The electrostatic energy difference is $\Delta\Delta\mathcal{F}_\phi = -14.2\,\text{kcal/mol}$, which means Na^+ is favored in this part, since it is EN in the filter due to the smaller size. These two values are consistent with the values calculated from ϕ_{S2} in Eq. (12) in Ref. [43], which adopts a Poisson-Fermi model with nonlocal electrostatics. Overall, K^+ has a high selectivity by the competition of the two parts.

B. K^+/Ca^{2+} selectivity

In this subsection, we consider the case with three ions K^+, Ca^{2+} (or Ba^{2+}) and Cl^- (respectively c_1, c_2, and c_3), and study the selectivity between K^+ and Ca^{2+} (or Ba^{2+}).

In this case, one can not directly analyze the ratio c_1/c_2 anymore, since they have different valences. Due to the factor z_i^2 in ΔW_i in Eq. (14), the barrier $\Delta W_2 \approx 549$ for Ca^{2+} is much larger. Now, we consider the EN case in the filter:

$$c_1 + 2c_2 - c_3 = q. \tag{37}$$

With the help of Eqs. (9) and (10), this is a cubic equation for e^ϕ and once ϕ is solved all c_i can be recovered. The analytic solution for ϕ is quite complicated, and involves many exponentially large and small terms. One cannot get the correct answer unless making proper approximations in different situations by keeping only the leading exponential terms and neglecting the high-order exponential terms. There are two situations. When q satisfies Eq. (18), we get the same approximation as in Eq. (20), and similarly the ratio c_1^*/c_2^* for the selectivity of K^+ and Ca^{2+} is exponentially large.

When q is relatively large,

$$\frac{1}{a_1^3\delta} < q < \frac{2}{a_2^3\delta}, \tag{38}$$

we know in the previous K^+/Na^+ case that the maximum amount $1/a_1^3\delta$ of K^+ can not balance q in filter, however, with the presence of divalent ions such as Ca^{2+}, this is feasible. The other critical value $2/a_2^3\delta$ is just the maximum effective charge that Ca^{2+} can provide in the limited space of filter. In this case, the EN condition Eq. (37) gives the leading-order

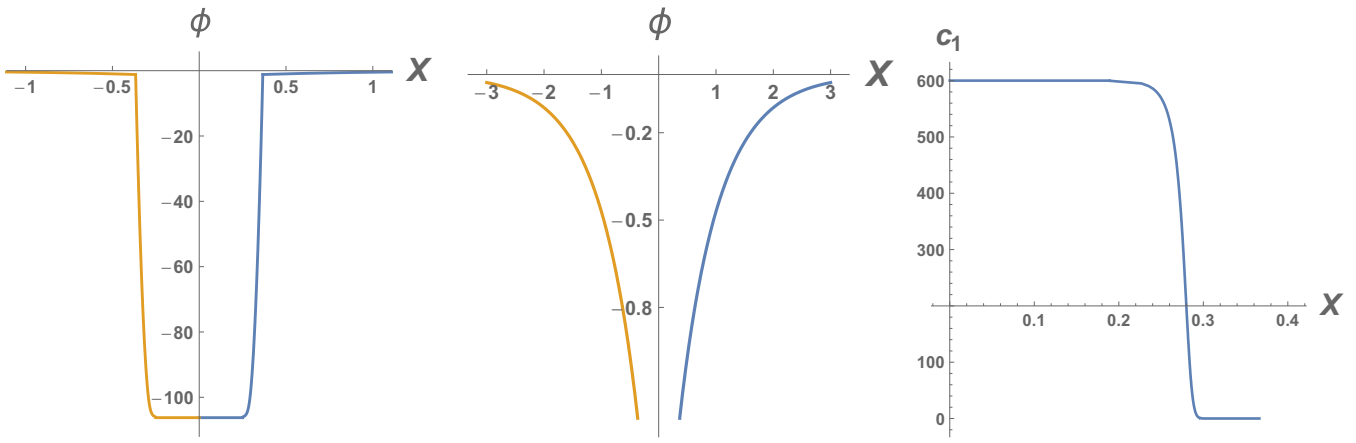

(a) (b) (c)

FIG. 5. The profiles for the case $q = 600 < 1/a_1^3\delta$: (a) ϕ in both filter and chamber, (b) ϕ in the chamber, (c) c_1 in the right-half interval of the filter.

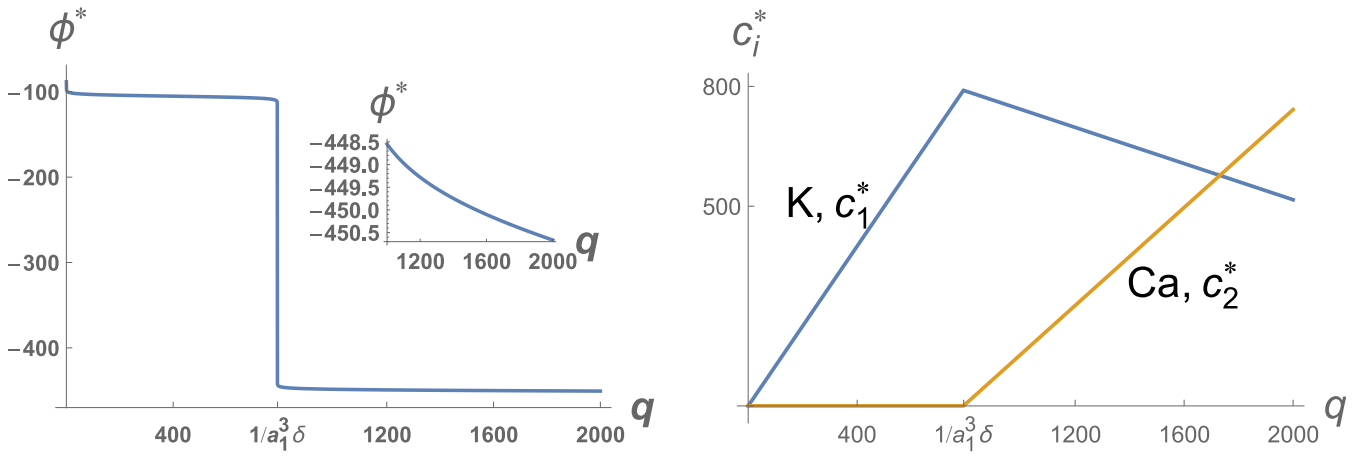

FIG. 6. Dependence of ϕ^* and c_i^* $(i = 1, 2)$ in the filter on effective charge q.

solution

$$c_1^* = \frac{2 - a_2^3 q\delta}{(2a_1^3 - a_2^3)\delta}, \quad c_2^* = \frac{a_1^3 q\delta - 1}{(2a_1^3 - a_2^3)\delta}, \quad c_3^* = 0,$$
$$\phi^* = B_2 - W_2(0) - [B_1 - W_1(0)] - \log c_2^* + \log c_1^*$$
$$= \Delta W_1 - \Delta W_2 + \log c_{2b} - \log c_{1b} + \phi_b$$
$$- \log\left(a_1^3 q\delta - 1\right) + \log\left(2 - a_2^3 q\delta\right). \tag{39}$$

In the above, ϕ^* depends on the calculated c_1^* and c_2^*, and therefore the size effect on ϕ^* is through these two quantities. The boundary conditions can affect ϕ^*, but have negligible influence on the concentrations c_1^* and c_2^* in the filter. Under normal physiological conditions [i.e., $c_{ib}, \phi_b \sim O(1)$] in the chamber, the selectivity of K^+ and Ca^{2+} for the case Eq. (38) is implied by the ratio

$$\frac{c_1^*}{c_2^*} = \frac{2 - a_2^3 q\delta}{(a_1^3 q\delta - 1)\delta}. \tag{40}$$

The selectivity in this case is determined by the effective permanent charge q and ion sizes, and the ratio in Eq. (40) becomes smaller with increase of q. In terms of free energy, Ca^{2+} is more favored by increase of q, because Ca^{2+} can make filter region electro-neutral and reduce the electrostatic energy. This conclusion on selectivity also applies to the nonequilibrium case.

Remark. In the above approximation Eq. (39), c_1^* and c_2^* are determined by the constraints

$$c_1^* + 2c_2^* = q, \quad \delta\left(a_1^3 c_1^* + a_2^3 c_2^*\right) = 1. \tag{41}$$

This implies that the EN condition is satisfied, and at the same time the filter is saturated with K^+ and Ca^{2+}. These two combined effects determine concentrations of K^+ and Ca^{2+}. It further implies, in the case of Eq. (38), that the concentration of K^+ itself can not balance q in the filter. Since Ca^{2+} has a larger valence, in spite of its larger Born solvation energy, the filter needs to recruit Ca^{2+} (by squeezing out some K^+ at the same time) to help out the electrostatic balancing.

Figure 6 shows the dependence of the above solution Eq. (39) on q, with $c_{1b} = c_{2b} = 1$, $\phi_b = 0$ and data in Eq. (A3) of Appendix A. The first part of the curves is the same as in Figure 2, when $q < 1/a_1^3\delta \approx 790$. When q exceeds this critical value, the concentration of Ca^{2+} increases while that of K^+ decreases. When q crosses the critical value, the minimum value ϕ^* in the filter transitions from the previous state at about -55 to another state at about -225, see the embedded figure in Fig. 6(a). Based on the data Eq. (A3) in Appendix A, the next critical value for saturation of c_2 is $q = 2/a_2^3\delta \approx 4280$. Figure 6 does not reach this value.

Barium Ba^{2+} has often been used to block K^+ channel [38,64,65], via electrostatic stabilization in the permeation pathway. At high concentrations of external K^+, the block-time distribution of Ba^{2+} is double exponential, implying at least two Ba^{2+} binding sites in the SF [38]. This coexistence of Ba^{2+} and K^+ inside the SF was observed in MD computation [6] with Ba^{2+} at binding site S2 and K^+ at binding site S0 forming a lock-in state impeding the translocation of Ba^{2+} [66].

For this case, the size of Ba^{2+} is larger than Ca^{2+}, given in Appendix A. Since it also has $+2$ valence, the energy barrier ($\approx$402) is still much larger than that of K^+. The above analysis still holds, and Fig. 7 shows the results and dependence on q, with same data as before. In this case, the next critical value is $q = 2/a_{\mathrm{Ba}}^3\delta \sim 1688$. Figure 7(b) indicates that Ba^{2+} is more effective to block K^+ due to its larger size.

Remark. The above analysis is also valid for the case with four ions: K^+, Na^+, Ca^{2+} (or Ba^{2+}), and Cl^-. Based on the analysis in Sec. III A, the concentration of Na^+ is always exponentially smaller than K^+. Thus, K^+ is favored compared with Na^+, and adding Na^+ will make no difference. The non-EN case will not be discussed here, since for relatively large q the two ions K^+ and Ca^{2+} can coexist to maintain EN. For even larger $q > 2/a_2^3\delta$ or near transition point $q = 1/a_1^3\delta$, we need to consider the non-EN case. The analysis is similar to Sec. III A 2, except that we have a more complicated $G(\phi)$ in Eq. (31) for such a case.

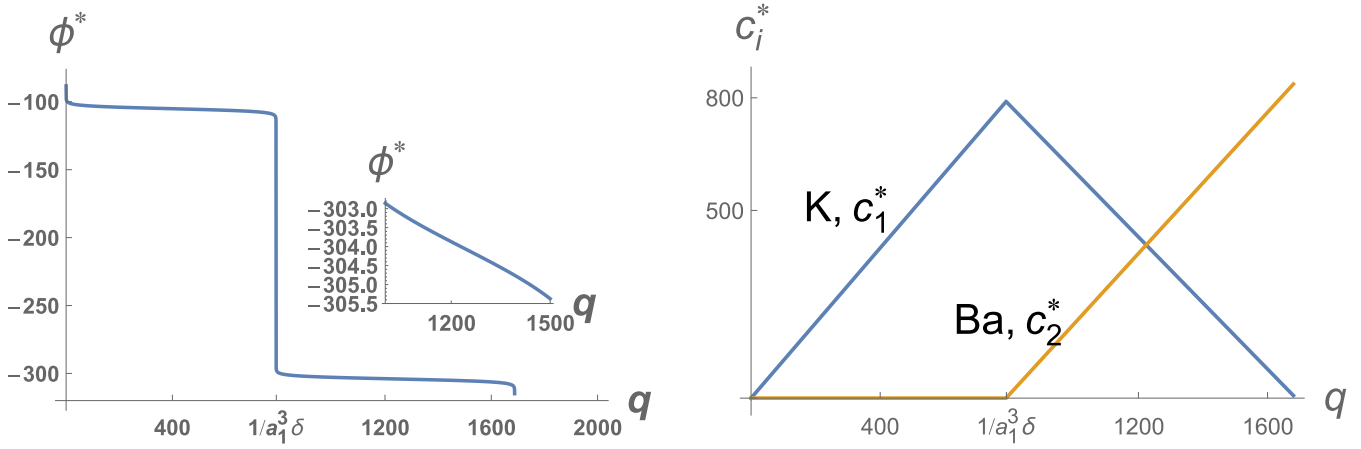

(a) (b)

FIG. 7. Dependence of ϕ^* and c_i^* $(i = 1, 2)$ in the filter on effective charge q.

IV. NONEQUILIBRIUM CASE AND FLUX-VOLTAGE RELATION

In this section, we assume the same concentrations at the two ends of the chamber but with different electric potential. This gives rise to variation in electrochemical potential μ_i across the interval $x \in [-1, 1]$, which induces fluxes. We intend to study the flux-voltage relations at steady state for the previous two cases. This section is restricted to a relatively long chamber region (length L_b), where the analytical flux-voltage relations are available. For general cases, numerical or semianalytical solutions will be shown in the next sections.

A. Fluxes of K^+/Na^+ case

In this subsection, we consider the three-ion case with K^+, Na^+, and Cl^-. At the two ends $x = \pm 1$, we impose

$$c_1(\pm 1) = 1, \quad c_2(\pm 1) = c_{2b}, \quad c_3(\pm 1) = 1 + c_{2b},$$
$$\phi(-1) = V, \quad \phi(1) = 0. \tag{42}$$

In this case, the results in Sec. III A about selectivity of K^+ and Na^+ are still valid. Although B_i in Eq. (10) is not an exact constant anymore, the variation is small since μ_i is monotone. We have also pointed out in Sec. III A that c_2 is exponentially small unless c_2 is 10^{15} times larger than that of c_1 near the filter. Based on results on selectivity, we now estimate the relative variations $\Delta\mu_i$ for each μ_i $(i = 1, 2, 3)$ in the chamber and the filter. Since in the chamber it is almost the classical PNP system, we get $c_i \sim O(1)$, implying

$$\Delta\mu_i = O(J_i), \quad \text{in the chamber.} \tag{43}$$

In the filter, we have that either $c_i \sim O(q)$ or c_i is exponentially small. Since the filter interval is small, as a first approximation by Eq. $(5)_3$, we have

$$\Delta\mu_i \approx \frac{L_f J_i}{D_i A_f c_i^*}, \quad \text{in the filter.} \tag{44}$$

We know that the total variation [sum of Eqs. (43) and (44)] from the left end to the right end is $O(1)$ with $V \sim O(1)$. From Sec. III A, we have $c_1^* \sim O(q)$ in the filter, and by the data Eqs. (A3) and (A4) in Appendix A we get the estimate

$$\frac{L_f}{D_1 A_f c_1^*} \sim 10^{-3}\text{–}10^{-2}. \tag{45}$$

This implies that $J_1 \sim O(1)$, and the filter region can be neglected for variation of μ_1. However, c_2^* and c_3^* are exponentially small in the filter, thus J_2 and J_3 can only be exponentially small, but this still gives finite variations $\Delta\mu_2$, $\Delta\mu_3$ in the filter by Eq. (44). In this context, we can treat $J_2 = J_3 = 0$ when studying the chamber region, and therefore we only need to concentrate on the J_1-V relation.

Remark. In this paper, for simplicity, we have adopted the same diffusion coefficient D_i $(i = 1, ..., n)$ for each ion in the filter and chamber regions. In a modified PNP model [57], the diffusion coefficients are modified to depend on concentrations. In Refs. [42,44,67–69], it is suggested that D_i in the filter region might be smaller than that in the chamber region, with the ratio in the range of 1/2–1/10. The ratio 1/4.7 is adopted for the gradmicidin A channel in a PNP-Fermi model [44], and the ratio about 0.7–0.9 is adopted for the KcsA channel in Brownian dynamics computation [70]. The ratio of D_i will only appear in the estimates in Eqs. (44) and (45), but since it is $O(1)$ this will have little impact on these estimates and later results for the I-V relations. In addition, for the equilibrium case, the values of diffusion constants will not affect the analysis and the conclusions on selectivity in Sec. III.

In the chamber, it is eligible to use the EN condition as first approximation for the relatively long chamber. We take constant cross sectional area $A(x) = 1$ for illustration. By neglecting the $O(\delta)$ term, we get the classic system

$$c_1'(x) + c_1\phi'(x) = -J_1/D_1 \equiv -J,$$
$$c_2'(x) + c_2\phi'(x) = 0,$$
$$c_3'(x) - c_3\phi'(x) = 0,$$
$$c_1 + c_2 = c_3. \tag{46}$$

This can be solved explicitly for the left half chamber $-1 < x < 0$ and the right half chamber $0 < x < 1$, given in

Appendix B. Here, $x = 0$ is treated as the filter. By the continuity of μ_1 at the filter, we get (see Appendix B)

$$\log\left[\frac{(1+c_{2b}-J/2)^2}{1+c_{2b}}-c_{2b}\right]+V = \log\left[\frac{(1+c_{2b}+J/2)^2}{1+c_{2b}}-c_{2b}\right], \tag{47}$$

which provides the J-V relation. This can be obtained by solving a quadratic equation, and we select the reasonable root that satisfies $J = 0$ at $V = 0$,

$$J = \frac{2(1+c_{2b})(1+e^V)-2\sqrt{1+c_{2b}}\sqrt{4e^V+c_{2b}(1+e^V)^2}}{e^V-1}. \tag{48}$$

For the special case $c_{2b} = 0$, we have

$$J = \frac{2(e^{V/2}-1)}{(e^{V/2}+1)}. \tag{49}$$

The general case of $A(x)$ causes no essential problem (see Appendix B), and we finally get

$$J\int_{L_f/2}^{1}\frac{1}{A(s)}ds = \frac{2(1+c_{2b})(1+e^V)-2\sqrt{1+c_{2b}}\sqrt{4e^V+c_{2b}(1+e^V)^2}}{e^V-1}. \tag{50}$$

Since $L_f \sim O(\epsilon)$, for special case $A(x) = 1$, the integral factor after J on the left-hand side degenerates to $1 - L_f/2 \approx 1$, and therefore Eq. (48) is recovered. Similarly with general $D_1(x)$, the left-hand side of Eq. (50) is replaced by $J_1\int_{L_f/2}^{1}\frac{1}{D_1(s)A(s)}ds$.

Remark. We have used the EN condition in the above system, which causes an $O(\epsilon J)$ error in estimates of the variation $\Delta\mu_1$, due to the classical BL near the filter edge in the chamber (see Ref. [71]). Also in Eq. (48), there is an $O(\epsilon)$ error caused by treating the filter as a point $x = 0$ as the filter length is $O(\epsilon)$. But in Eq. (50) the exact point $x = L_f/2$ of the filter edge is used. Later numerical calculations show that the above approximation is good for small V, and it slightly underestimates the flux for relatively large V.

Figure 8 shows the J-V relations (note $J_1 = D_1 J$) in Eq. (50) with $A = 1$ and different boundary concentrations c_{2b}. It indicates that the flux J tends to saturate for relatively large V (the reason will be illustrated in Sec. VI), which agrees well with experimental observations [13]. The presence of Na^+ reduces or blocks the flux of K^+, but the tendency to saturate at large V remains the same. These generally agree well with experiment measurements in Ref. [13] except that there is a dip in the experimental I-V curves at moderate V corresponding to the block by Na^+, which becomes relieved at high V by a "punch-through" mechanism.

Figure 9 shows the profiles of $\phi(x)$ and $c_i(x)$ $(i = 1, 2, 3)$ with boundary values $c_{2b} = 0.1, V = 1$ in Eq. (42) and parameter $q < 1/a_1^3\delta$. The choice of $q < 1/a_1^3\delta$ is for illustration purpose as ϕ in most part of the filter is approximated by ϕ^*. The exact values of q and ϕ^* are not used in Figure 9 because they are so large, and the red dashed vertical lines indicate a large jump to the two values. For larger $q > 1/a_1^3\delta$

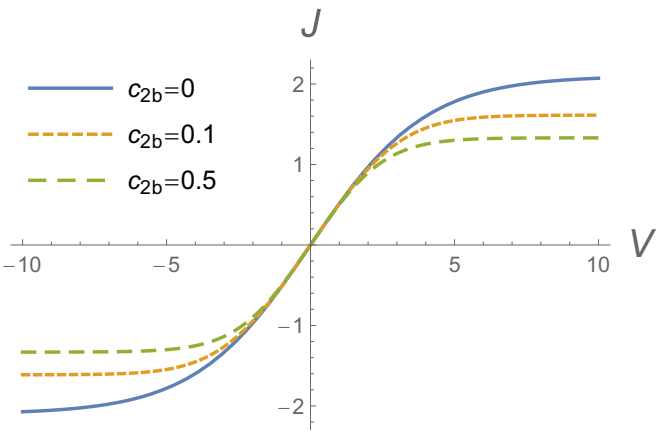

FIG. 8. Flux-voltage J-V relations with different boundary concentrations c_{2b}.

the results will not change much except that ϕ in the filter has a profile like Fig. 4(a). Figure 10 shows the profiles of $\mu_i(x)$ $(i = 1, 2, 3)$ for each ion species. There is finite variation for μ_1 in the chamber, which causes the finite flux of c_1. The μ_2 and μ_3 are constant in the chamber, leading to 0 fluxes. Even though there is finite variation for μ_2 and μ_3 in the filter, there is no flux since the concentrations c_2 and c_3 are essentially 0 in the filter.

Now we summarize the strategy for determining the J_i-V relations, which also applies to other cases such as the next subsection.

(1) From the equilibrium case, determine which ions (here K^+, in the next subsection K^+ and Ca^{2+}) are prevalent in the filter and which (here Na^+ and Cl^-) are 0 in the filter.

(2) Set finite flux for only those ions prevalent in the filter and set 0 flux for others, and then solve the equations for the left and right chamber regions.

(3) Determine the J_i-V relations by using the continuity of μ_i at the filter for only those ions prevalent in the filter (other μ_i are constants in the chamber and have jumps at the filter).

It appears that we have only used the chamber equations to approximate the J_i-V relations, but actually it is totally different to directly solve the chamber equations without the filter. In that case, the chamber solutions of ϕ, c_i $(i = 1, 2, 3)$ will be continuous and all the fluxes J_i and variation of all μ_i would be finite and not 0. For the present case with the filter, the chamber solutions of ϕ, c_i $(i = 1, 2, 3)$ in Fig. 9 have jumps at the filter, and the μ_2 and μ_3 in Fig. 10 are constants in each chamber. The saturation of J-V curve here can not be captured without the filter.

B. Fluxes of K^+/Ca^{2+} case

In this subsection, we consider the three-ion case with K^+, Ca^{2+}, and Cl^- (the case for Ba^{2+} is similar). At the two ends $x = \pm 1$, we impose

$$c_1(\pm 1) = 1, \quad c_2(\pm 1) = c_{2b}, \quad c_3(\pm 1) = 1 + 2c_{2b}, \quad \phi(-1) = V, \quad \phi(1) = 0. \tag{51}$$

The analysis on the variation of $\Delta\mu_i$ $(i = 1, 2, 3)$ is similar to the preceding subsection, and we can follow the same strategy to determine the flux-voltage relations. Depending on the

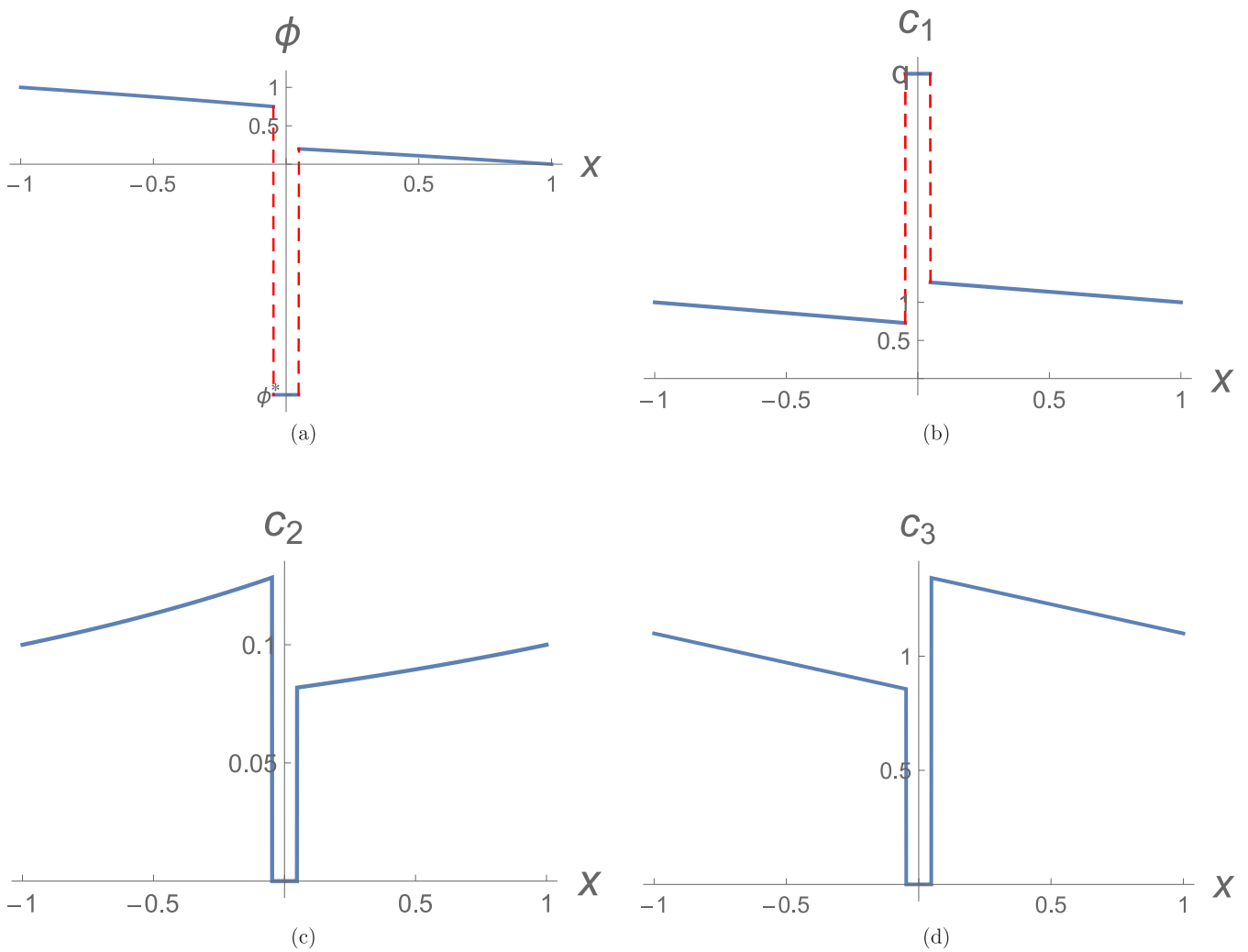

FIG. 9. Profiles of $\phi(x)$ and $c_i(x)$ $(i = 1, 2, 3)$ with $c_{2b} = 0.1, V = 1$.

parameter q and results in Sec. III B about selectivity of K^+ and Ca^{2+}, there are two cases. (1) When $q < 1/a_1^3\delta$, we get $J_2 = 0, J_3 = 0$ and finite J_1. The results of the J_1-V relation will then be similar to those in the preceding subsection, and the profiles of c_i and μ_i $(i = 1, 2, 3)$ are similar; hence, we do not repeat them here. (2) When $1/a_1^3\delta < q < 2/a_2^3\delta$ is relatively large as in Eq. (38), we have $J_3 = 0$ and finite J_1 and J_2, since K^+ and Ca^{2+} can coexist in the filter.

Now we focus on the second case and take $A(x) = 1$ for illustration. We solve the following system in the chamber:

$$\begin{aligned} \partial_x c_1 + c_1 \partial_x \phi &= -J_1/D_1 \equiv \tilde{J}_1, \\ \partial_x c_2 + 2c_2 \partial_x \phi &= -J_2/D_2 \equiv \tilde{J}_2, \\ \partial_x c_3 - c_3 \partial_x \phi &= 0, \\ c_1 + 2c_2 - c_3 &= 0. \end{aligned} \tag{52}$$

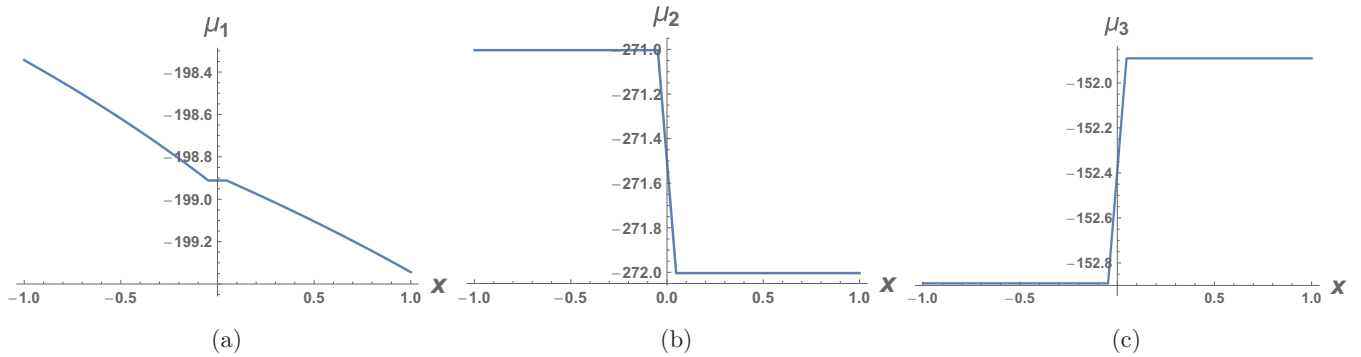

FIG. 10. Profiles of $\mu_i(x)$ $(i = 1, 2, 3)$ with $c_{2b} = 0.1, V = 1$.

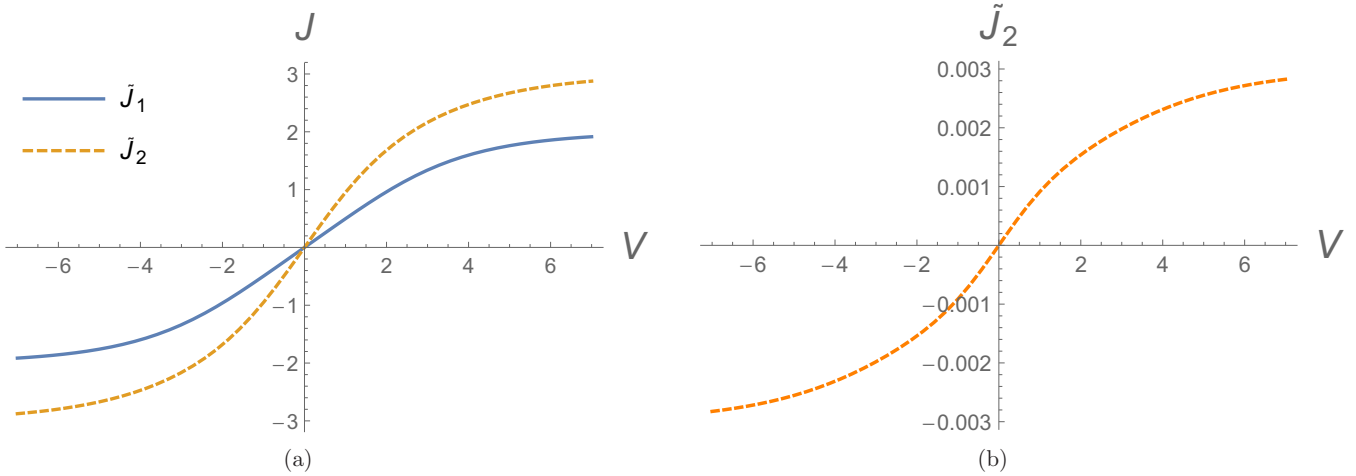

FIG. 11. Flux-voltage relations with (a) $c_{2b} = 1$, (b) $c_{2b} = 10^{-3}$.

It is not straightforward to solve $\phi(x)$ and $c_i(x)$ $(i = 1, 2, 3)$ directly, instead if we treat ϕ as the independent variable, then we can solve $x(\phi)$ and $c_i(\phi)$ $(i = 1, 2, 3)$ explicitly. We denote solutions by $x_R(\phi)$, $c_{iR}(\phi)$ for the right half interval $0 < x < 1$ and by $x_L(\phi)$, $c_{iL}(\phi)$ for $-1 < x < 0$, given in Appendix B. By the continuity of μ_1 and μ_2 at $x = 0$, we get

$$\begin{aligned} \phi_{0L} + \ln c_{1L}(\phi_{0L}) &= \phi_{0R} + \ln c_{1R}(\phi_{0R}), \\ 2\phi_{0L} + \ln c_{2L}(\phi_{0L}) &= 2\phi_{0R} + \ln c_{2R}(\phi_{0R}), \end{aligned} \tag{53}$$

where ϕ_{0L} and ϕ_{0R} are the left and right limit values of ϕ at $x = 0$, which are defined by

$$x_L(\phi_{0L}) = 0, \quad x_R(\phi_{0R}) = 0. \tag{54}$$

All these four equations involve the fluxes $\tilde{J}_1, \tilde{J}_2$ and voltage V, thus they determine $\tilde{J}_1, \tilde{J}_2, \phi_{0L}, \phi_{0R}$ in terms of V. The general case of $A(x)$ needs only slight modifications, see Appendix B.

Figure 11(a) shows the flux-voltage relations with $c_{2b} = 1$, indicating that both fluxes $\tilde{J}_1$ and $\tilde{J}_2$ saturate for relatively large V. Figure 11(b) shows the flux $\tilde{J}_2$ when $c_{2b} = 10^{-3}$ is set to be very small, indicating that the flux almost proportionally gets smaller as the chamber concentration gets smaller. In Fig. 11(b), the flux $\tilde{J}_1$ is omitted since it is almost the same as in Fig. 11(a) and of much larger scale. Figure 12 shows the profiles of $\phi(x)$ and $c_i(x)$ $(i = 1, 2, 3)$ with boundary values $c_{2b} = 1, V = 1$ and parameter $1/a_1^3 < q < 2/a_2^3\delta$. Figure 13 shows the profiles of $\mu_i(x)$ $(i = 1, 2, 3)$ for each ion species. The finite variations of μ_1 and μ_2 in the chamber induce the finite fluxes of c_1 and c_2, while μ_3 is constant in the chamber, leading to 0 flux of c_3.

V. COMPUTATIONAL ANALYSIS

In this section, we solve the modified PNP system numerically. Our main objective is to verify the preceding analysis under simplifying conditions.

We use the dynamic process to simulate the steady state solutions for ϕ, c_i and associated fluxes. Smooth dimensionless functions $\epsilon_r(x)$ (connecting 1/40 and 1) and $A(x)$ (connecting 1/30 and 1) will be used in the simulation, see Fig. 14. Now we illustrate the process by considering the 3-ions case with c_i $(i = 1, 2, 3)$ for K^+, Na^+, and Cl^-. This is to verify the previous analytical results for both equilibrium and nonequilibrium cases. We adopt the initial conditions at $t = 0$,

$$c_1(x, 0) = 1, \quad c_2(x, 0) = 0.1, \quad c_3(x, 0) = 1.1. \tag{55}$$

The boundary conditions are

$$\begin{aligned} c_1(\pm 1, t) = 1, \quad c_2(\pm 1, t) = 0.1, \quad c_3(\pm 1, t) = 1.1, \\ \phi(-1) = V, \quad \phi(1) = 0. \end{aligned} \tag{56}$$

First, we set $V = 0$ and compare the numerical results with analytical results in Eq. (20) (or Fig. 2). A series of cases with different q are simulated. In the simulation, a finite-volume method is used with nonuniform mesh points. More mesh points are used in the filter, near the filter edge, and in regions with large gradient of ϵ_r. There are totally 273 points. A very small time step (because of the large q, small ϵ and small mesh size) is chosen to ensure stability and accuracy of the algorithm. After about 20 h on a computer (processor: 4 GHz, i76700K; memory: 32 GB), the solution tends to a steady state (i.e., all fluxes are almost 0). The profiles of ϕ and c_i $(i = 1, 2, 3)$ for $q = 600$ are shown as red curves in Fig. 15, in comparison with the analytical results shown in blue curves from Sec. III. The numerical and analytical solutions agree very well except a smoothing region near the two edges of the filter. For instance, the constant values of ϕ in the filter show remarkable agreement, i.e., $\phi^* = -106.2303, -106.2319$ in numerical and analytical results. One can see that K^+ is favored in the filter region, and all the other ions are essentially 0 in the filter region. This agrees with results in Eq. (20). To see clearly the dependence on q, the profiles of ϕ for different q are shown in Fig. 16(a), showing that it is constant in the filter region. In Figs. 16(b) and 16(c), the constant values of ϕ, c_1, c_2 in the filter are compared with previous analytical results, where curves are from the previous Fig. 2 and dots are from numerical results.

We have also tested different smoothing profiles of $\epsilon_r(x)$ and $A(x)$ and boundary conditions for concentrations. As long as ϵ_r is 1/40 (original value is 2 before scaling) in middle part

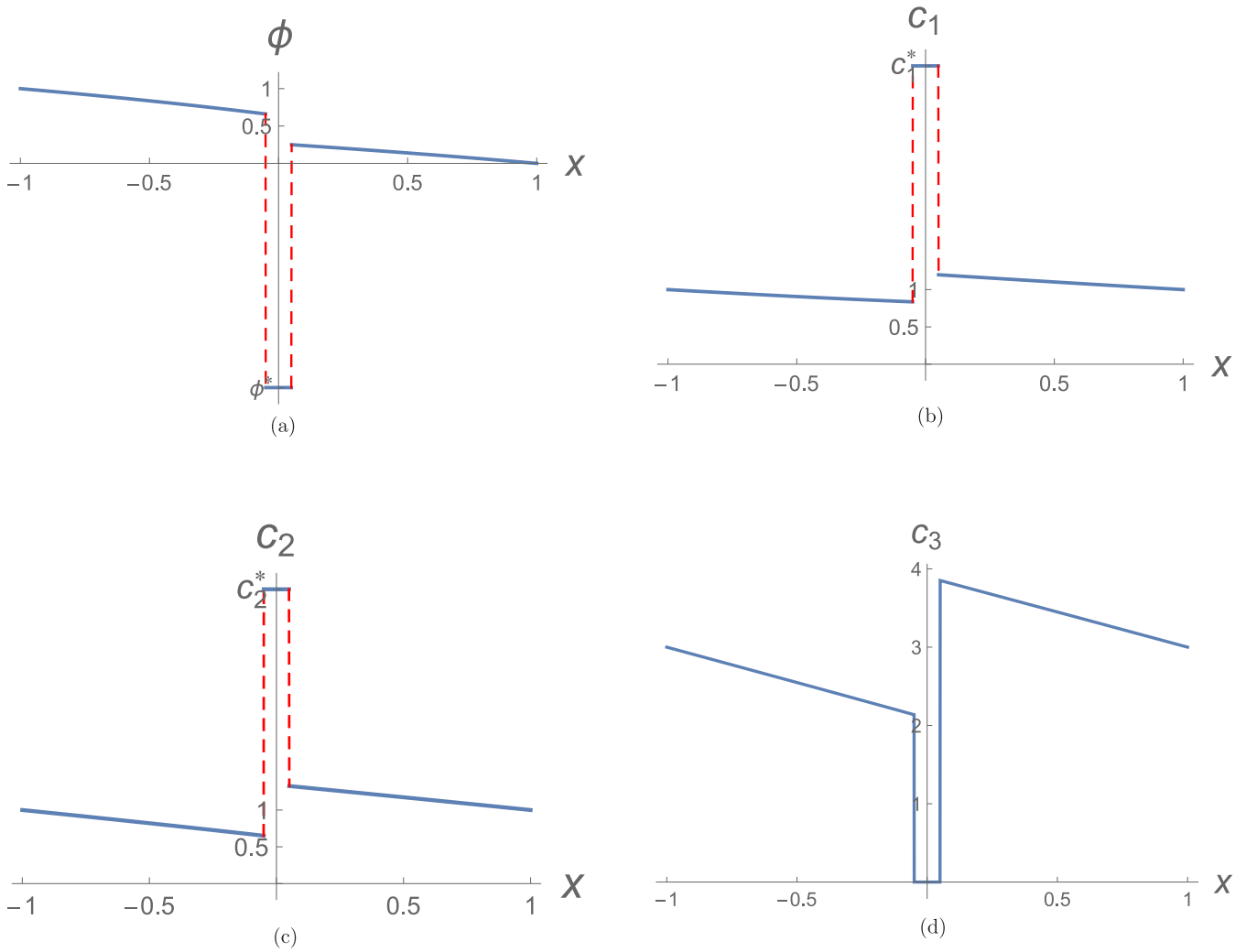

FIG. 12. Profiles of $\phi(x)$ and $c_i(x)$ $(i = 1, 2, 3)$ with $c_{2b} = 1$, $V = 1$ and $1/a_1^3 < q < 2/a_2^3\delta$.

of the filter, the minimum value of ϕ will not change. This also verifies the predictions in Eq. (20).

To test the analysis of the nonequilibrium case, we set $V = 1$, $q = 600$ and others the same as above. After computation of about 20 h to $t = 2$, the system tends to a steady state. The fluxes are shown in Fig. 17, indicating that only flux J_1 is nonzero and goes to a constant 1.211 at steady state. This feature agrees with the previous analysis. The previous predicted flux by Eq. (50) with $A(x) = 1$, $c_{2b} = 0.1$ is $J \approx 0.51$, and hence $J_1 = D_1 J \approx 1$. They differ by $O(\epsilon)$ with present $\epsilon \approx 0.13$, as it is natural for the previous approximation. In addition, the difference is partly due to the the smoothing of $\epsilon_r(x)$ and $A(x)$. The profiles of c_i, ϕ $(i = 1, 2, 3)$ are shown in Fig. 18. Some features are similar to the equilibrium case, but the profiles are no longer symmetric. The numerical solutions in the chamber are also compared with previous analytical

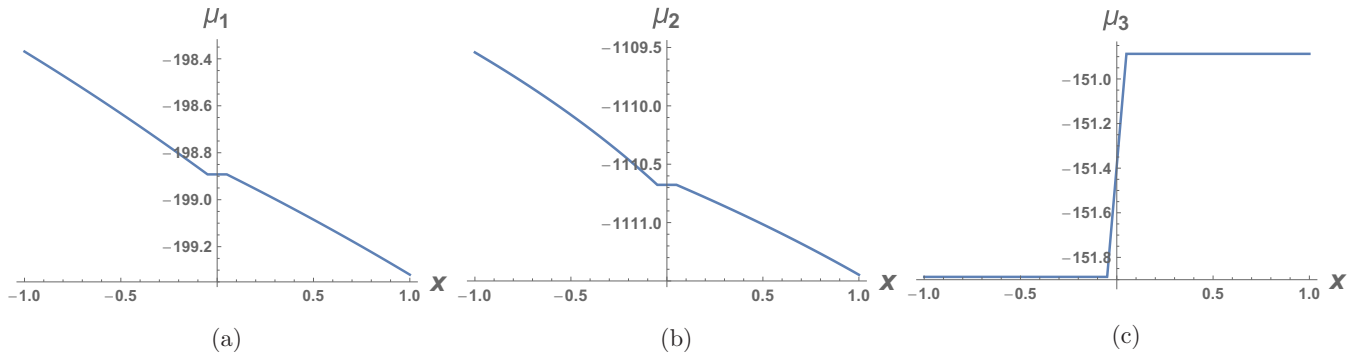

FIG. 13. Profiles of $\mu_i(x)$ $(i = 1, 2, 3)$ with $c_{2b} = 1$, $V = 1$ and $1/a_1^3 < q < 2/a_2^3\delta$.

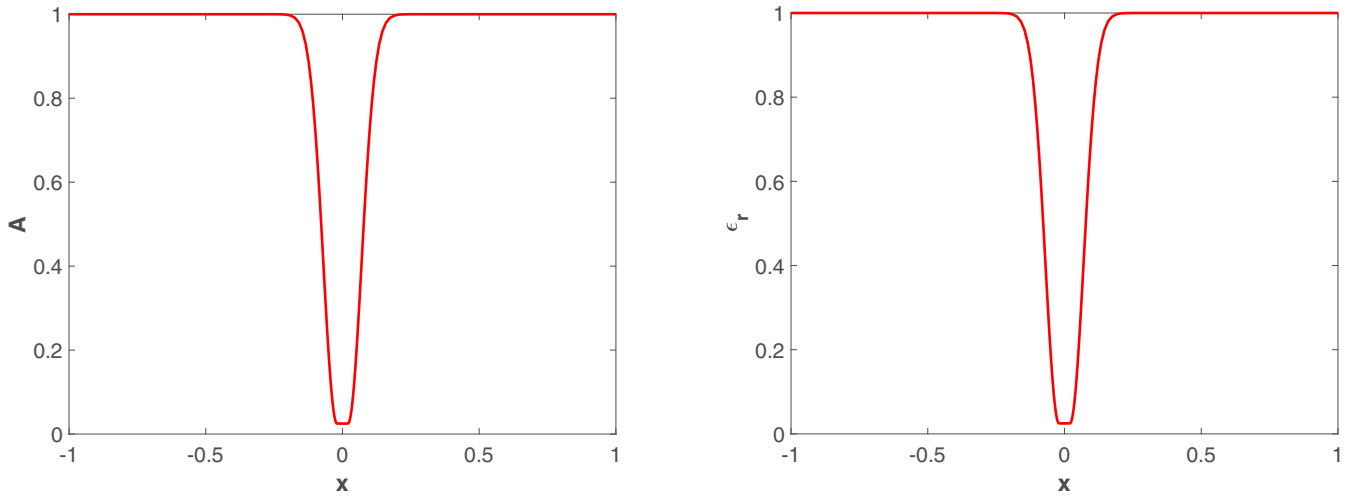

(a) (b)

FIG. 14. Smooth functions $A(x)$ and $\epsilon_r(x)$ used in simulation.

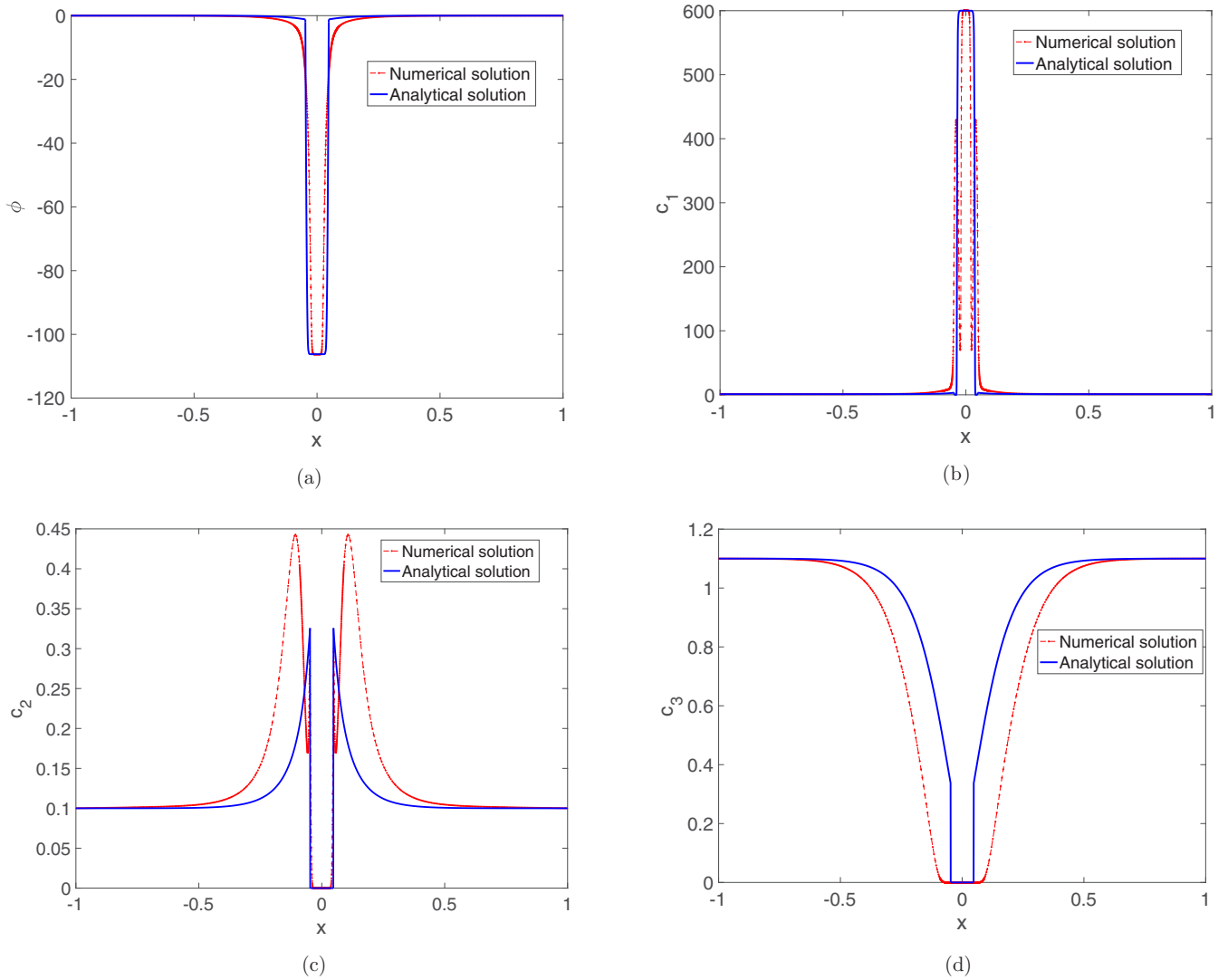

(a) (b) (c) (d)

FIG. 15. Profiles of ϕ and c_i $(i = 1, 2, 3)$ near steady state for $V = 0$ and $q = 600$.

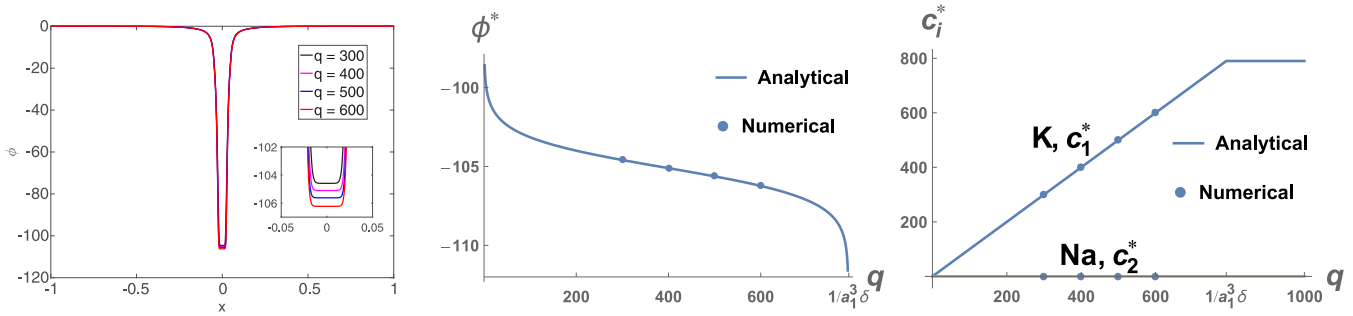

(a) (b) (c)

FIG. 16. Profiles of ϕ at steady state for $V = 0$ and different q and comparison with analytical results in Fig. 2.

solutions (see Fig. 9 and Appendix B) in dashed lines of embedded figures. The profiles of μ_i $(i = 1, 2, 3)$ are shown in Fig. 19. All profiles of c_i, ϕ, μ_i $(i = 1, 2, 3)$ except μ_3 show agreement with previous analytical results. We have also tested different V, and compared with analytical flux-voltage curves in Fig. 21 in the next section.

Now we provide some insight and explanation for the above incorrect μ_3, based on previous analytical results. One can easily prove that μ_3 is monotone in steady state by the positivity of c_3. Thus, Fig. 10(c) is correct and the numerical result in Fig. 19(c) is incorrect. By definition of μ_3 and matching with the boundary conditions (the two values of μ_3 at the boundaries do not differ much), in the filter we approximately have [cf. Eq. (28)]

$$\log c_3 - \log\left(1 - \sum_{k=1}^{3} c_k(x) a_k^3 \delta\right) \sim -75 + \phi \sim -181. \quad (57)$$

Since the second term is $O(1)$ for present $q = 600$ not exceeding the critical value of 790, we need c_3 to be as accurate as $e^{-181} \sim 10^{-79}$. We know it is almost 0, but to compute the correct μ_3 in the filter, it has to go to as small as 10^{-79}. This is partially verified numerically, i.e., when we increase the accuracy of c_3 in the filter, the values of μ_3 in the filter as in Fig. 19(c) will decrease further (in both cases $V = 0$ and $V = 1$). In addition, the accuracy of c_3 would also affect other results in the filter, to a certain degree. For example, if we only maintain accuracy up to 10^{-10}, then the minimum values of ϕ are incorrect (differ a great deal from the analytical results), but it works for ϕ when we maintain accuracy up to 10^{-15} [Fig. 16(b) is based on this]. The inaccuracy of μ_3 is also one reason that the profile of c_3 in Fig. 15 has a relatively large discrepancy with analytical results.

When Ca^{2+} is present and with the above $q = 600$, the results and features are very similar to the above results (omitted here). This agrees with the previous analysis. We also tried with large $q = 1000$ in the above 3-ion case and in a case with Ca^{2+}, but the computation is very unstable, failing to capture the features in analysis. Now we provide some explanation based the previous analysis and provide some insight on the numerical difficulty. In such cases, the ions saturate in the filter and thus the second term in μ_i of Eq. (6) is crucial, requiring very high accuracy for c_i in computation. For the 3-ion case with Ca^{2+} in Sec. III B, one can see that even for the simple case of the algebraic equations from Eq. (37) and Eqs. (9) and (10), it is not straightforward to determine ϕ. Originally, the solution depends on identity Eq. (10), and from the solution in Eq. (39) we find that in this case

$$\log\left(1 - \sum_{k=1}^{3} c_k(x) a_k^3 \delta\right) \sim -344. \quad (58)$$

This is the cause of the main difficulty of direct numerical computation, as this term is essential to capture the behavior in the filter. One should be very cautious to calculate c_i directly in simulation, since both Ca^{2+} and K^+ are in the order $O(q)$ but they need to be accurate to e^{-344} to capture this term. Other

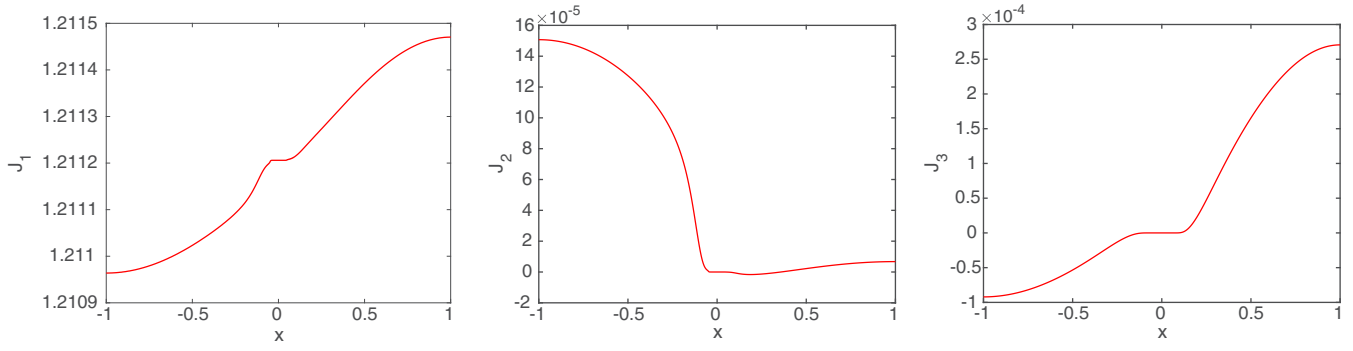

(a) (b) (c)

FIG. 17. The fluxes J_i $(i = 1, 2, 3)$ near steady state for $V = 1, q = 600$.

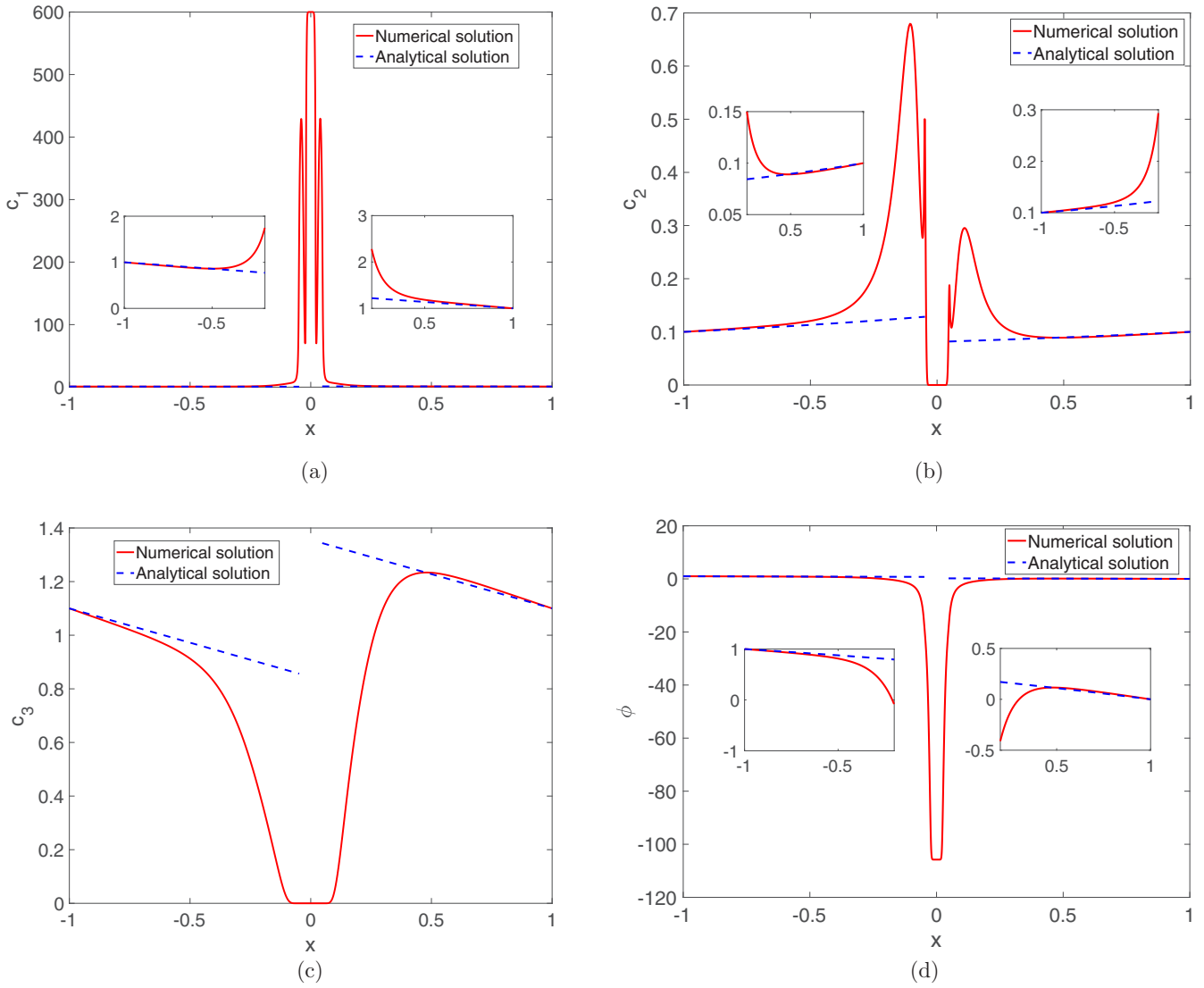

FIG. 18. The profiles of c_i $(i = 1, 2, 3)$ and ϕ near steady state, for $V = 1$, $q = 600$.

difficulty can also arise from the $\log c_i$ terms, as some ion like Cl^- is exponentially small (this is already illustrated in last paragraph for the previous case). These difficulties can be avoided if the c_i can be represented by ϕ, as ϕ is well behaved in analysis and computation. This can be done for the equilibrium case with the help of Eqs. (9) and (10), but is not straightforward in the nonequilibrium case.

We also briefly mention the 3-ion case of K^+, Na^+, Cl^- with large large q, as in Sec. III A 2. Similar difficulties arise from the two log terms in μ_i in Eq. (6). In addition, the

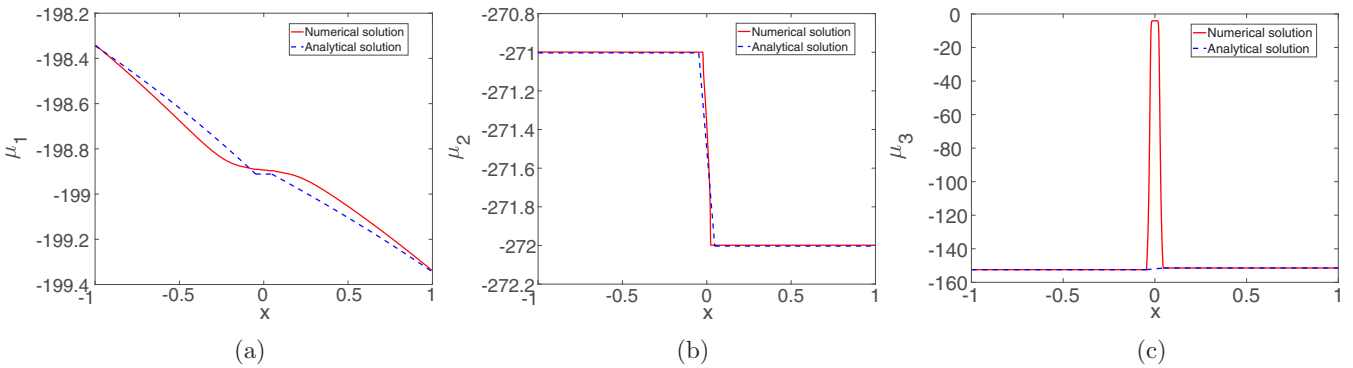

FIG. 19. The μ_i $(i = 1, 2, 3)$ near steady state for $V = 1$, $q = 600$.

analytical solution or Fig. 4(c) shows that there is an internal transition point for c_1 in the filter, where c_1 changes from exponentially small to $O(q)$. In some part of the filter, c_1 is exponentially small, and, however, $J_1 \sim c_1 \partial_x \mu_1$ should be finite. It is not easy to capture the transition or to compute the form $0 * \infty$.

VI. HYBRID METHOD

When q is large, direct numerical computation becomes challenging and inefficient. In addition, when ϵ is relatively large (i.e., short chamber length L_b), the analysis for the J_i-V relations in Sec. IV fails since the EN assumption is no longer valid in the chamber.

In this subsection, we provide an alternative hybrid method by combining the analysis in the filter with numerical computation in the chamber. We obtain an analytical solution in the filter for the nonequilibrium case by slightly modifying that from Sec. III A 2. In the chamber we can simplify the system, which is generally easy to solve numerically (no such difficulties mentioned in last section) or relates to some special functions. We could also call the solutions in this section semianalytical solutions.

We take the three ion case K^+, Na^+, and Cl^- as illustration, and assume $A = 1$ and $\epsilon_r = 1$ in the chamber (the general case should not cause any essential difficulty). The dimensional length can be either large or small (reflected in parameter ϵ), e.g., $L = 10.5$ nm in previous sections or $L = 3$ nm in more practical case. The system in the right chamber by neglecting $O(\delta)$ term is

$$\begin{aligned} &c_1'(x) + c_1\phi'(x) = -J_1/D_1 \equiv -J, \\ &c_2'(x) + c_2\phi'(x) = 0, \\ &c_3'(x) - c_3\phi'(x) = 0, \\ &-\epsilon^2\phi''(x) = c_1 + c_2 - c_3, \quad s < x < 1, \end{aligned} \tag{59}$$

with boundary conditions $c_i = c_{ib}$, $\phi = 0$ at $x = 1$. Here, the position s denotes the edge of the filter. We immediately get c_2, c_3 in terms of ϕ,

$$c_2 = c_{2b}e^{-\phi}, \quad c_3 = c_{3b}e^{\phi}, \tag{60}$$

so that

$$-\epsilon^2\phi''(x) = c_1 + c_{2b}e^{-\phi} - c_{3b}e^{\phi}, \quad s < x < 1. \tag{61}$$

Multiplying ϕ' on this equation and using Eq. $(59)_1$, we obtain

$$\begin{aligned} c_1(x) = \epsilon^2 \tfrac{1}{2}\{[\phi'(x)]^2 - [\phi'(1)]^2\} - J(x-1) \\ + c_{1b} - c_{2b}(e^{-\phi} - 1) - c_{3b}(e^{\phi} - 1). \end{aligned} \tag{62}$$

Substituting into Eq. (61) and with $c_{1b} + c_{2b} = c_{3b}$, we obtain

$$\begin{aligned} \epsilon^2\phi''(x) = -\tfrac{1}{2}\epsilon^2\{[\phi'(x)]^2 - [\phi'(1)]^2\} \\ + J(x-1) + 2c_{3b}(e^{\phi} - 1), \quad s < x < 1. \end{aligned} \tag{63}$$

Similarly for the left chamber with boundary conditions $c_i = c_{ib}$ and $\phi = V$, we would have

$$\begin{aligned} \epsilon^2\phi''(x) = -\tfrac{1}{2}\epsilon^2\{[\phi'(x)]^2 - [\phi'(-1)]^2\} + J(x+1) \\ + 2c_{3b}(e^{\phi - V} - 1), \quad -1 < x < s. \end{aligned} \tag{64}$$

These two equations are to be solved with help of the solution in the filter or with some matching connection conditions at the edge of the filter.

Remark. The final differential equation for ϕ seems complicated, but actually it relates to a special function, defined by Painlevé II (PII) equation. Here we would like to bring attention to this connection, as Painlevé transcendents have been studied intensively in past few decades [72]. The reduction of steady state PNP system with ± 1 ions to PII equation was mentioned in Ref. [51]. For the present 3-ion case, it is similar and we can adopt the transform

$$\begin{aligned} y = \frac{e^{\phi/2}}{\sqrt{2}(\epsilon J)^{1/3}}, \quad z = \frac{Jx + C}{2(\epsilon J)^{2/3}}, \\ C = -J + \frac{1}{2}\epsilon^2[\phi'(1)]^2 - 2c_{3b}, \end{aligned} \tag{65}$$

so that Eq. (63) becomes a PII equation with parameter 0,

$$y''(z) = 2y^3 + zy. \tag{66}$$

The typical solutions in the present setting are that $\phi(x)$ either blows up to ∞ or to $-\infty$ at $x = x^*$ as x decreases from 1. This agrees with the features (like poles) of the solutions of PII equations. The reasonable solution in the current case, however, is connected to the filter solution at $x = s$ before it reaches x^*.

Next we would like to connect the above chamber solutions with the filter solution. We take $q > 1/a_1^3\delta$ for example. In general, for the nonequilibrium case, one can not express c_i in terms of ϕ and then directly construct the solution like Sec. III A 2. We, however, make use of the fact that Eq. (9) still holds in the nonequilibrium case. In addition, for selected ions (K^+ or K^+ and Ca^{2+}), μ_i are constants for the filter region based on evidence from both analysis and simulation. Thus, the only modification of the filter solution in Eqs. (30) and (31) is that the constant B_1 is replaced by $\mu_1(s)$, which relates to the chamber solution. We can determine the solutions by using a shooting method. For the right chamber, once we fix J and $\phi'(1)$, we can compute the solution of ϕ by Eq. (63) and hence c_i ($i = 1, 2, 3$) up to $x = s$. We treat the solution as a special function of arguments $J, \phi'(1)$. With the calculated $B_1 = \mu_1(s)$ in Eqs. (30) and (31), the filter solution is known. Then, the connection conditions at $x = s$ are

$$\begin{aligned} A_f\sqrt{2\epsilon_{r0}[G(\phi_s) - G(\phi_0)]} = \epsilon\phi'(s), \quad \phi_s = \phi(s), \\ \sqrt{\frac{\epsilon_{r0}}{2}}\int_{\phi_0}^{\phi_s} \frac{1}{\sqrt{G(\phi) - G(\phi_0)}}d\phi = (s - s_0)/\epsilon, \end{aligned} \tag{67}$$

where s_0 is the position of the minimum of ϕ (i.e., when $\phi' = 0$) in the filter. Similarly for the left chamber, with given V, J and $\phi'(-1)$, we can compute the solution of ϕ in both the chamber and filter regions. Then, the connection conditions at $x = -s$ are

$$\begin{aligned} A_f\sqrt{2\epsilon_{r0}[G(\phi_{-s}) - G(\phi_0)]} = -\epsilon\phi'(-s), \quad \phi_{-s} = \phi(-s), \\ \sqrt{\frac{\epsilon_{r0}}{2}}\int_{\phi_0}^{\phi_{-s}} \frac{1}{\sqrt{G(\phi) - G(\phi_0)}}d\phi = (s + s_0)/\epsilon. \end{aligned} \tag{68}$$

Note that we have $s_0 = 0$ for the equilibrium case $V = 0$, but in general the solution is not exactly symmetric. The final

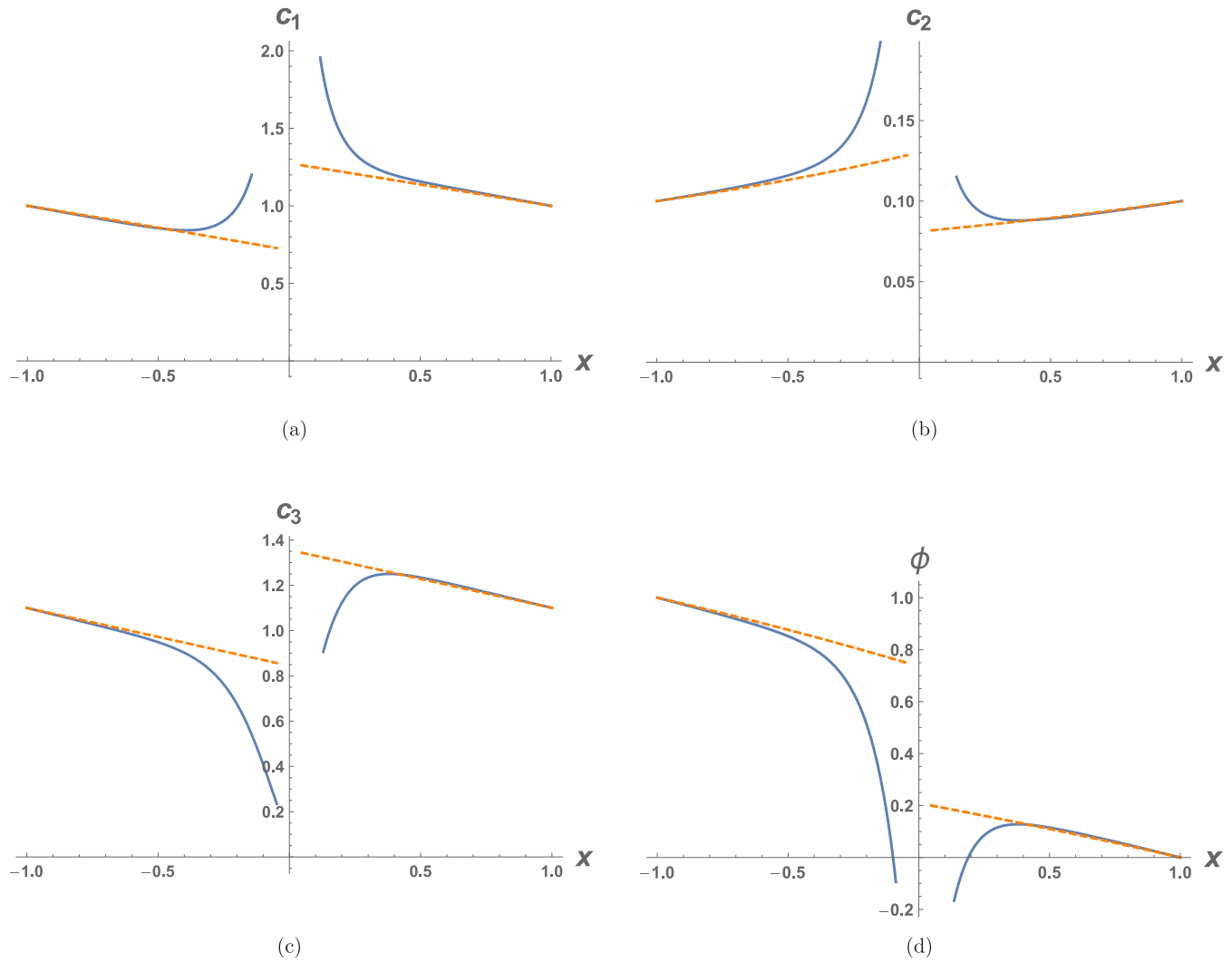

FIG. 20. The profiles of c_i $(i = 1, 2, 3)$ and ϕ with $V = 1$ and $q = 600$.

condition is

$$\mu_1(s) = \mu_1(-s). \tag{69}$$

In brief, with given boundary value V, we have seven nonlinear equations for seven unknowns ϕ_0, $\phi(\pm s)$, $\phi'(\pm 1)$, J and s_0. The case $q < 1/a_1^3\delta$ is simpler, and we do not need the two integral conditions Eq. $(68)_3$ and Eq. $(69)_3$ anymore, which are replaced by

$$\phi_0 = \mu_1(s) - W_1(0) + \log\left(1 - a_1^3 q\delta\right) - \log q. \tag{70}$$

Then, we have six nonlinear equations for six unknowns ϕ_0, $\phi(\pm s)$, $\phi'(\pm 1)$ and J.

The above algorithm can be implemented in Mathematica (or Matlab) with only a few lines of code, the solutions for given V can be computed by finding the roots of the six or seven nonlinear equations. The computation is very efficient, and the solution is found within seconds on a laptop (processor: 1.6 GHz, i5; memory: 4 GB). This is verified with $V = 0$, $q = 1000$ and data in Eq. (A3), and it coincides with previous results in Sec. III A 2. For the previous case $q = 600$, $V = 1$ in Sec. IV A, the solutions are computed for comparison. The profiles of ϕ and c_i $(i = 1, 2, 3)$ are shown in Fig. 20 with dashed lines from the previous analytical solution, showing good agreement away from the filter. One can clearly see the BL near the filter edge in the profiles, which is ignored in previous analytical results. The flux computed here is $J \approx 0.56$ (or $J_1 \approx 1.10$), also indicating that the previous approximation $J \approx 0.51$ in Sec. IV A slightly underestimates the flux.

Remark. There is a fictitious singularity in the integrals in Eqs. (67) and (68), i.e., the integrand is singular at $\phi = \phi_0$, but the integral is of the form $\int_0^a \frac{1}{\sqrt{x}} dx$. We have used a little trick in practical computation to ensure stability and accuracy, i.e., replace ϕ_0 by $\phi_0 + \delta_0$, say $\delta_0 = 10^{-10}$. For quite small ϵ (long dimensional L) and large c_{2b}, the solution of ϕ is sensitive to the boundary conditions $\phi'(\pm 1)$. It can easily blow up to $\pm\infty$, and only a narrow interval of $\phi'(\pm 1)$ with given J leads to solution of ϕ in whole interval $[s, 1]$.

For different V, the flux-voltage (J-V or I-V) relations by three different methods are compared in Fig. 21(a), where red curve is from the current section, and dots and dashed lines are from the previous numerical and analytical solutions. Although different approximations regarding the BL near the filter or parameters $A(x)$, $\epsilon_r(x)$ are made, the three methods

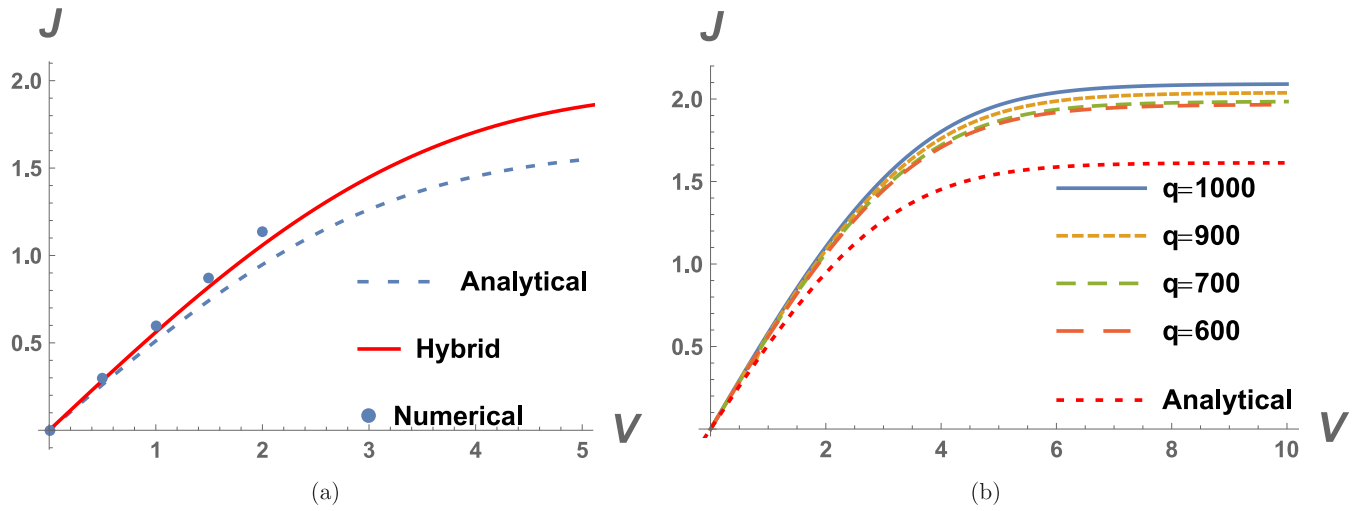

FIG. 21. The J-V relations with small ϵ (dimensional length $L = 10.5$ nm): (a) comparison of different methods (b) with different q.

provide similar results and trends for the J-V curve. The analytical solution underestimates the flux, due to neglect of the BL near the edge, while the slight difference between the numerical and hybrid methods are due to the smoothing of $\epsilon_r(x)$ and $A(x)$ used in the numerical solutions. For different q, the flux-voltage J-V relations are computed by varying V, shown in Fig. 21(b), with reference curve from the analytical result in Sec. IV A. The flux in each curve saturates for large V, and as q increases the flux will increase.

The saturation of flux is certainly a consequence of selectivity of the filter, which is originally due to parameters ϵ_r and q. Without the filter, the flux-voltage relations will be totally different, as indicated at the end of Sec. IV A. With the filter, the most important condition is continuity of μ_i for selected ions. To see the direct reason of saturation of flux for the K^+/Na^+ case, we analyze the profiles of c_1 in the chamber for different V, obtained by both analytical and hybrid methods. Figure 22 shows the profiles of c_1 with parameters $c_{2b} = 0.1, q = 600$ and three different V. The dashed lines from the analytical results provide reasonable approximation in the region away from the filter, but are not as accurate as the solid lines near the filter, which also capture the BL. Both indicate that c_1 approaches 0 near the left edge of the filter as V increases, and one can easily see this trend from the analytical expressions in Appendix B. The left edge of the filter is important here since the flux is from left to right with positive V (otherwise, we should analyze the right edge). As c_1 can not be negative, this is the main restriction for the saturation of scaled flux J. Also note that as the original flux J_1 is controlled by diffusion constant D_1, one may think the saturation is related to the diffusion limit [13,73]. When c_1 is near 0 at left edge, there are not enough ions available to go through the filter even with large V. When c_{2b} increases as in Figure 8, c_1 will be more likely to reach this critical value, resulting in smaller saturation flux J. The reason for saturation of both fluxes for the case with Ca^{2+} in Sec. IV B is similar, except that the two fluxes are restricted by values of both c_1 and c_2 at the edge of the filter (both approach 0 as V increases).

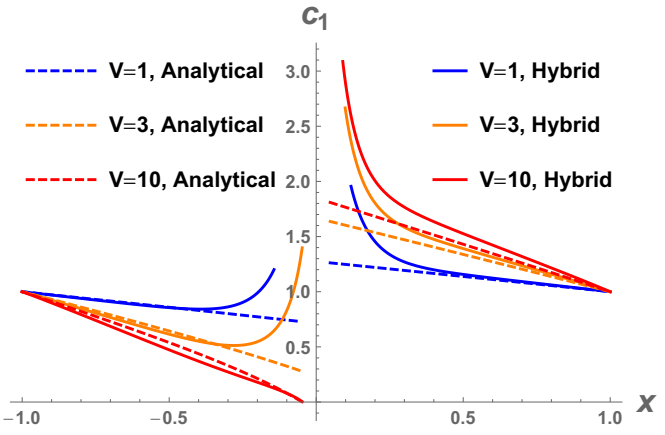

FIG. 22. The profiles of c_1 in the chamber for different V.

The hybrid method in this section has the advantages of both efficiency and accuracy for the J-V or I-V relation. The direct numerical computation is extremely time-consuming, even for one point in the J-V curve of Fig. 21(a). Thus it can hardly be used to compare I-V relations with experiments. The hybrid method can produce J-V curves very efficiently—about 20 min for one smooth curve in Fig. 21(b). It also includes the BL effect near the edge of the filter, and does not have the restriction for parameters (like ϵ or length L), in contrast to the analytical approximations. Thus it can be readily used to compare with experiments or estimate parameters in the model.

The data in Eq. (A3) of Appendix A corresponds to relatively long dimensional length $L = 10.5$ nm. In more realistic cases, however, L is much shorter based on the molecular structure of the KcsA channel. To compare with experiments, we adopt the dimensional length $L = 3$ nm (i.e., $L_b = 2.5$ nm), which leads to $\epsilon \approx 0.46$. Figure 23(a) shows the J-V relations for $c_{1b} = 1$ and different c_{2b} and q. As c_{2b} increases, the flux will decrease, while the flux will increase as q increases. From the present formulation, the dimensional

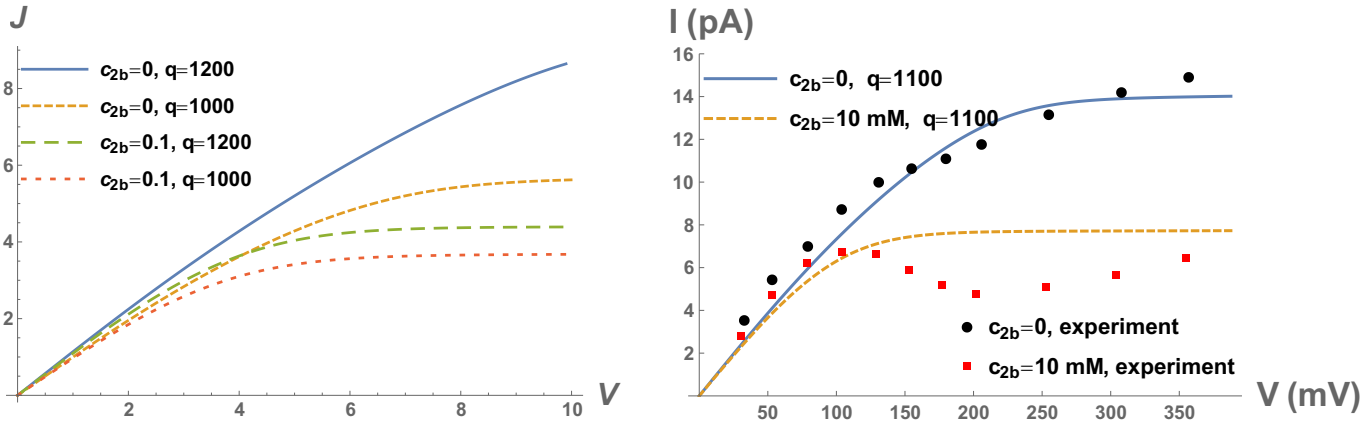

(a) (b)

FIG. 23. The J-V relations with different q, c_{2b} and relatively large ϵ (small dimensional length $L = 3$ nm): (a) dimensionless curves, (b) comparison with experiments.

flux and current are scaled by

$$\frac{A_b D_0 c_0}{L} = 6.02 \times 10^6/\text{s}, \quad \frac{e_0 A_b D_0 c_0}{L} = 0.96\,\text{pA}, \tag{71}$$

where $L = 3$ nm is used. Note also $J_1 = D_1 J$ where $D_1 = 1.96$. Figure 23(b) shows the I-V relations with physical units for $q = 1100$, which agrees with experimental data in Ref. [13], where dots are extracted from Fig. 2B of Ref. [13]. The two curves show similar order and profiles to those of experiments, except a dip in the experimental data for $c_{2b} = 10$ mM. One could also make the results more comparable by adjusting other parameters, e.g., the cross sectional area $A(x)$.

The idea in this section can be applied to more general cases, e.g., with general $A(x)$ and $D_i(x)$, slowly varying $\epsilon_r(x)$ in the chamber, and with divalent ions such as Ca^{2+}. The formulation and solution process are quite similar, except that we might solve more than one equation in the chamber region. We will not repeat this here.

VII. CONCLUDING REMARKS

We have studied the selectivity of KcsA potassium channel and the I-V relation. With a 1D modified PNP system by keeping the essential elements, many features of the channel have been demonstrated by both analytical formulas and numerical simulations. The selectivity among K^+ and other ions are clearly illustrated with analytical formulas. Saturation of the I-V curve is captured by various methods, and explanations are provided. We hope the methods in the current work can be applied to more accurate structures and other types of ion channels, and will provide insights into the selectivity and I-V relations. More work is needed to make comparison with experiments or calibrate some parameters in the model for different channels. The analysis and computation under high-dimensional framework is ongoing as an extension of the current work.

ACKNOWLEDGMENTS

This work is partially supported by NSERC (CA) and the Fields Institute and was initiated when T.-L.H. visited the Fields Institute as a Fields Research Fellow. The authors thank the reviewers for their constructive comments, which lead to a much improved paper, and a careful proofread of the manuscript by Nathan Gold.

APPENDIX A: PARAMETER VALUES

The data in this Appendix are mainly from Refs. [1,32,71,74]. For dimensional system, the vacuum permittivity ϵ_0, elementary charge e_0, Boltzmann constant k_B, and absolute temperature T are

$$\epsilon_0 = 8.854 \times 10^{-12}\,\text{C/(V m)}, \quad e_0 = 1.602 \times 10^{-19}\,\text{C},$$
$$k_B = 1.38 \times 10^{-23}\,\text{J/K}, \quad T = 300\,\text{K}. \tag{A1}$$

Some typical values are adopted as

$$\phi_0 = \frac{k_B T}{e_0} \approx 24\,\text{mV}, \quad c_0 = 100\,\text{mM} = 6.022 \times 10^{25}\,\text{m}^{-3},$$
$$D_0 = 10^{-9}\,\text{m}^2/\text{s}, \quad a_0 = 3\,\text{Å}, \quad L_b = 10\,\text{nm}, \quad L_f = 1\,\text{nm},$$
$$L = 10.5\,\text{nm}, \quad \epsilon_{rb} = 80, \quad \epsilon_{rf} = 2, \quad A_b = 30\,\text{Å}^2,$$
$$a_{\text{K}} = 2.76\,\text{Å}, \quad a_{\text{Na}} = 2.04\,\text{Å}, \quad a_{\text{Ca}} = 1.98\,\text{Å},$$
$$a_{\text{Cl}} = 3.62\,\text{Å}, \quad a_{Ba} = 2.70\,\text{Å}. \tag{A2}$$

If we think of an exact sphere instead of a cube, then the factor $(\pi/6)^{1/3} \approx 0.8$ should be multiplied to the above effective ion diameters a_i. The length L_b could be smaller, if we consider a shorter chamber.

For dimensionless system, we have the estimates of dimensionless parameters

$$\epsilon \approx 0.13, \quad \delta = a_0^3 c_0 \approx 1.6 \times 10^{-3},$$
$$W_0 = \frac{e^2}{8\pi\epsilon_0 a_0 k_B T} \approx 187, \quad \frac{1}{40} \leqslant \epsilon_r \leqslant 1, \quad A_f \leqslant A \leqslant 1,$$
$$L_f = 0.095, \quad D_{\text{K}} = 1.96, \quad D_{\text{Na}} = 1.33, \quad D_{\text{Ca}} = 0.79,$$

$$D_{\rm Cl}=2.03,\quad a_{\rm K}=0.92,\quad a_{\rm Na}=0.68,\quad a_{\rm Ca}=0.66,$$
$$a_{\rm Cl}=1.21,\quad a_{\rm Ba}=0.9. \tag{A3}$$

The permanent charge and cross sectional area are estimated from a 3D Poisson-Boltzmann computation based on the realistic molecular structure of KcsA. The corresponding dimensionless quantities for q and A_f are

$$q\sim 10^3,\quad \text{e.g.,}\quad [1000,2000],$$
$$A_f\sim\frac{1\,\text{Å}^2}{30\,\text{Å}^2}=\frac{1}{30}. \tag{A4}$$

APPENDIX B: SOME SOLUTIONS AND EXPRESSIONS

From definition Eq. (6), we get

$$\frac{c_i}{1-\sum_{k=1}^n \delta c_k a_k^3}=e^{\mu_i-W_i-z_i\phi},\quad i=1,..,n, \tag{B1}$$

then by multiplication of a_i and summation, we obtain

$$\frac{C}{1-C\delta}=\sum_{i=1}^n a_i^3 e^{\mu_i-W_i-z_i\phi}\equiv F,\quad C=\sum_{i=1}^n c_i a_i^3, \tag{B2}$$

which implies

$$C=\frac{F}{1+F\delta},\quad c_i=\frac{e^{\mu_i-W_i-z_i\phi}}{(1+F\delta)}. \tag{B3}$$

The solution of Eq. (26) in the chamber region is given by

$$\phi(X)=2\log\left(\frac{e^{\sqrt{2}X}+m}{e^{\sqrt{2}X}-m}\right),$$
$$m=\frac{e^{\sqrt{2}S}(e^{\phi_s/2}-1)}{e^{\phi_s/2}+1},\quad S<X<\infty. \tag{B4}$$

For the system Eq. (46), we get for the left-half chamber $-1<x<0$,

$$c_3(x)=1+c_{2b}-\frac{J}{2}(x+1),\quad \phi(x)=\log\frac{c_3(x)}{1+c_{2b}}+V,$$
$$c_2(x)=\frac{c_{2b}(1+c_{2b})}{c_3(x)},\quad c_1(x)=c_3(x)-c_2(x), \tag{B5}$$

and for the right-half chamber $0<x<1$,

$$c_3(x)=1+c_{2b}-\frac{J}{2}(x-1),\quad \phi(x)=\log\frac{c_3(x)}{1+c_{2b}},$$
$$c_2(x)=\frac{c_{2b}(1+c_{2b})}{c_3(x)},\quad c_1(x)=c_3(x)-c_2(x). \tag{B6}$$

Based on the solutions, we get $\mu_1(x)$ for the left chamber

$$\begin{aligned}\mu_1(x)&=\log c_1+\phi+W_1\\&=\log\left(c_3(x)-\frac{c_{2b}(1+c_{2b})}{c_3(x)}\right)+\log\frac{c_3(x)}{1+c_{2b}}+V+W_1\\&=\log\left(\frac{c_3^2(x)}{1+c_{2b}}-c_{2b}\right)+V+W_1\\&=\log\left(\frac{\left[1+c_{2b}-\frac{J}{2}(x+1)\right]^2}{1+c_{2b}}-c_{2b}\right)+V+W_1,\end{aligned} \tag{B7}$$

substituting $x=0$ give the left-hand side of Eq. (47) except the W_1 term.

For general $A(x)$, the linear terms $x+1, x-1$ in $c_3(x)$ in Eqs. (B5) and (B6) should be replaced by

$$\int_{-1}^x\frac{1}{A(s)}ds,\quad \int_1^x\frac{1}{A(s)}ds, \tag{B8}$$

and all the other expressions are the same. The final result for the J-V relation in Eq. (48) is almost the same except that J is multiplied by a factor $\int_{L_f/2}^1\frac{1}{A(s)}ds$.

The system Eq. (52) is equivalent to a system for functions of ϕ

$$\dot c_1+c_1=-\tilde J_1\dot x,\quad \dot c_2+2c_2=-\tilde J_2\dot x,$$
$$\dot c_3-c_3=0,\quad c_1+2c_2-c_3=0, \tag{B9}$$

where dot represents derivative with respect to ϕ. Then the solutions $x_R(\phi)$ and $c_{iR}(\phi)$ $(i=1,2,3)$ for the right-half interval $0<x<1$ (i.e., $\phi_{0R}<\phi<0$ or $0<\phi<\phi_{0R}$) are

$$\begin{aligned}c_{3R}(\phi)&=(2c_{2b}+1)e^{\phi},\\c_{2R}(\phi)&=\frac{(3c_{2b}\tilde J_1-2\tilde J_2)e^{\lambda\phi}}{3\tilde J_1+4\tilde J_2}+\frac{2(2c_{2b}+1)\tilde J_2 e^{\phi}}{3\tilde J_1+4\tilde J_2},\\\lambda&=-\frac{2(\tilde J_1+\tilde J_2)}{\tilde J_1+2\tilde J_2},\quad c_{1R}(\phi)=c_{3R}(\phi)-2c_{2R}(\phi),\\x_R(\phi)&=1+\frac{3c_{2b}+2}{\tilde J_1+\tilde J_2}-\frac{6(2c_{2b}+1)e^{\phi}}{3\tilde J_1+4\tilde J_2}\\&\quad+\frac{(3c_{2b}\tilde J_1-2\tilde J_2)e^{\lambda\phi}}{(\tilde J_1+\tilde J_2)(3\tilde J_1+4\tilde J_2)}.\end{aligned} \tag{B10}$$

The solutions $c_{iL}(\phi)$ and $x_L(\phi)$ for the left-half interval $-1<x<0$ (i.e., $V<\phi<\phi_{0L}$ or $\phi_{0L}<\phi<V$) are

$$c_{iL}(\phi)=c_{iR}(\phi-V),\quad i=1,2,3,$$
$$x_L(\phi)=x_R(\phi-V)-2. \tag{B11}$$

For the general case of $A(x)$, one only needs to make a transformation $y=\int_{\pm1}^x\frac{1}{A(s)}ds$ for the right and left chamber equations. The only modifications of the above solutions are

$$y_R(\phi)=\frac{3c_{2b}+2}{\tilde J_1+\tilde J_2}-\frac{6(2c_{2b}+1)e^{\phi}}{3\tilde J_1+4\tilde J_2}+\frac{(3c_{2b}\tilde J_1-2\tilde J_2)e^{\lambda\phi}}{(\tilde J_1+\tilde J_2)(3\tilde J_1+4\tilde J_2)},$$
$$y_L(\phi)=y_R(\phi-V). \tag{B12}$$

For flux voltage relations, the equations in Eq. (53) will not change and the equations in Eq. (54) change to

$$y_R(\phi_{0L})=\int_1^{L_f/2}\frac{1}{A(s)}ds,\quad y_L(\phi_{0L})=\int_{-1}^{L_f/2}\frac{1}{A(s)}ds. \tag{B13}$$

APPENDIX C: THE FREE ENERGY

The free energy is given by

$$\mathcal{F}(c_1,..,c_n,\phi)=\mathcal{F}_\phi+\mathcal{F}_c+\mathcal{F}_w, \tag{C1}$$

and

$$\begin{aligned}\mathcal{F}_\phi &= \int_\Omega \left[-\frac{1}{2}\epsilon_0\epsilon_r|\nabla\phi|^2 + e_0\phi\left(\sum_{i=1}^n z_i c_i - q\right)\right]dv \\ &= \int_\Omega \frac{1}{2}e_0\phi\left(\sum_{i=1}^n z_i c_i - q\right)dv \\ \mathcal{F}_c &= k_B T\int_\Omega \left[\sum_{i=1}^n c_i \log\left(c_i a_i^3\right) + \frac{1-\sum_{i=1}^n c_i a_i^3}{a_0^3}\right. \\ &\quad \left.\times \log\left(1-\sum_{i=1}^n c_i a_i^3\right)\right]dv, \\ \mathcal{F}_w &= \int_\Omega \sum_{i=1}^n c_i W_i dv, \end{aligned} \tag{C2}$$

where $dv = A(x)dx$ is the volume element and a_0 is the diameter of water molecule. The three parts $\mathcal{F}_\phi$, $\mathcal{F}_c$, and $\mathcal{F}_w$ represent the electrostatic energy, the energy due to entropy of ions, and the solvation energy. The modified PNP system in Sec. II can be derived from this free energy, with a simplification of a factor a_i^3/a_0^3 in μ_i of Eq. (2). The energy is scale by k_BT in dimensionless form.

In the literature, ion selectivity is often defined by the free-energy difference between ions in a binding site relative to the corresponding quantity in the chamber. The above free energy will be used to compute the energy differences for Na^+ or K^+ from the chamber to the filter. Let c_1 denote Na^+ or K^+, and c_2 denote Cl^-. The data in Appendix A are adopted. The initial state is without the filter (or the filter is closed), and c_1 and c_2 are in electroneutral state in the chamber. The dimensionless values are

$$c_1 = c_2 = 2.55, \quad \phi = 0, \quad \text{in the chamber.} \tag{C3}$$

At the far end of the chamber, $\phi = 0$ and the EN condition are maintained, and the nonflux condition is used for c_1. Thus with the filter open, c_1 will redistribute and some can enter the filter. The equilibrium sate can be obtained by analytical solutions in Sec. III A 2. The energy difference for one ion from the chamber to the filter is defined by

$$\Delta\mathcal{F} = \frac{\mathcal{F}^{\text{equilibrium}} - \mathcal{F}^{\text{initial}}}{\int_{\text{filter}} c_1 dv}, \tag{C4}$$

and by Eq. (C1) the three parts $\Delta\mathcal{F}_\phi$, $\Delta\mathcal{F}_c$, $\Delta\mathcal{F}_w$ in $\Delta\mathcal{F}$ can be similarly defined. The selectivity of K^+ and Na^+ in MD simulations is defined as the difference of $\Delta\mathcal{F}$ between the two cases, we thus follow their notation to define

$$\Delta\Delta\mathcal{F}(K^+ \to Na^+) = \Delta\mathcal{F}(Na^+) - \Delta\mathcal{F}(K^+). \tag{C5}$$

Similarly, the constituting parts $\Delta\Delta\mathcal{F}_\phi$, $\Delta\Delta\mathcal{F}_c$, $\Delta\Delta\mathcal{F}_w$ are defined, in particular, $\Delta\Delta\mathcal{F}_w$ is consistent with difference in solvation energy in Eqs. (14) and (16),

$$\Delta\Delta\mathcal{F}_w = \Delta W(Na^+) - \Delta W(K^+) = 133.1 - 98.4 = 34.7, \tag{C6}$$

in dimensionless value.

With $q = 950$, it is non-EN in the filter for the case of KCl, and the profiles of solutions are like Fig. 4. While Na^+ has a smaller size, with $q = 950$ it is EN in the majority of the filter region for the case of NaCl, and the profiles of solutions are like Fig. 5. With these analytical solutions, the energy differences in dimensionless values are obtained

$$\Delta\Delta\mathcal{F}_\phi = -23.6, \quad \Delta\Delta\mathcal{F}_c = -0.7. \tag{C7}$$

To compare with the values in MD simulations, we multiply the scale k_BTN_A (N_A is for a mole of ions) and convert the unit of energy from J to kcal, and finally obtain

$$\begin{aligned}\Delta\Delta\mathcal{F}_w &= 20.8\,\text{kcal/mol}, \\ \Delta\Delta\mathcal{F}_\phi &= -14.2\,\text{kcal/mol}, \\ \Delta\Delta\mathcal{F}_c &= -0.4\,\text{kcal/mol}, \\ \Delta\Delta\mathcal{F} &= 6.2\,\text{kcal/mol}. \end{aligned} \tag{C8}$$

[1] B. Hille *et al.*, *Ion Channels of Excitable Membranes*, Vol. 507 (Sinauer, Sunderland, MA, 2001).
[2] J. Zheng and M. C. Trudeau, *Handbook of Ion Channels* (CRC Press, Boca Raton, FL, 2015).
[3] R. MacKinnon, S. L. Cohen, A. Kuo, A. Lee, and B. T. Chait, Science **280**, 106 (1998).
[4] M. J. Ackerman and D. E. Clapham, N. Engl. J. Med. **336**, 1575 (1997).
[5] W. A. Catterall, Neuron **67**, 915 (2010).
[6] A. N. Thompson, D. J. Posson, P. V. Parsa, and C. M. Nimigean, Proc. Natl. Acad. Sci. USA **105**, 6900 (2008).
[7] D. Wu, PloS One **12**, e0186789 (2017).
[8] R. MacKinnon, Angew. Chem., Int. Ed. **43**, 4265 (2004).
[9] E. Gouaux and R. MacKinnon, Science **310**, 1461 (2005).
[10] D. A. Doyle, J. M. Cabral, R. A. Pfuetzner, A. Kuo, J. M. Gulbis, S. L. Cohen, B. T. Chait, and R. MacKinnon, Science **280**, 69 (1998).
[11] J. Åqvist and V. Luzhkov, Nature **404**, 881 (2000).
[12] C. Miller, Nature **414**, 23 (2001).
[13] C. M. Nimigean and C. Miller, J. Gen. Physiol. **120**, 323 (2002).
[14] Y. Zhou, J. H. Morais-Cabral, A. Kaufman, and R. MacKinnon, Nature **414**, 43 (2001).
[15] D. Gillespie and R. S. Eisenberg, Phys. Rev. E **63**, 061902 (2001).
[16] P. A. Markowich, *The Stationary Semiconductor Device Equations* (Springer Science & Business Media, Berlin, 2013).
[17] J. J. Jasielec, G. Lisak, M. Wagner, T. Sokalski, and A. Lewenstam, Electroanalysis **25**, 133 (2013).
[18] A. Singer and J. Norbury, SIAM J. Appl. Math. **70**, 949 (2009).
[19] Z. Song, X. Cao, and H. Huang, Phys. Rev. E **98**, 032404 (2018).
[20] A. Flavell, M. Machen, B. Eisenberg, J. Kabre, C. Liu, and X. Li, J. Comput. Electron. **13**, 235 (2014).
[21] Q. Zheng, D. Chen, and G.-W. Wei, J. Comput. Phys. **230**, 5239 (2011).

[22] T. A. van der Straaten, J. M. Tang, U. Ravaioli, R. S. Eisenberg, and N. Aluru, J. Comput. Electron. **2**, 29 (2003).
[23] T.-L. Horng, T.-C. Lin, C. Liu, and B. Eisenberg, J. Phys. Chem. B **116**, 11422 (2012).
[24] N. Gavish, Physica D: Nonlin. Phenom. **368**, 50 (2018).
[25] T.-C. Lin and B. Eisenberg, Commun. Math. Sci. **12**, 149 (2014).
[26] M. S. Kilic, M. Z. Bazant, and A. Ajdari, Phys. Rev. E **75**, 021503 (2007).
[27] J.-L. Liu and B. Eisenberg, J. Chem. Phys. **148**, 054501 (2018).
[28] G. Lin, W. Liu, Y. Yi, and M. Zhang, SIAM J. Appl. Dynam. Syst. **12**, 1613 (2013).
[29] D. Xie, J.-L. Liu, and B. Eisenberg, Phys. Rev. E **94**, 012114 (2016).
[30] T.-L. Horng, P.-H. Tsai, and T.-C. Lin, Comput. Math. Biophys. **5**, 142 (2017).
[31] J.-L. Liu and B. Eisenberg, J. Phys. Chem. B **117**, 12051 (2013).
[32] J.-L. Liu and B. Eisenberg, J. Chem. Phys. **141**, 22D532 (2014).
[33] J.-L. Liu and B. Eisenberg, J. Chem. Phys. **141**, 075102 (2014).
[34] B. Lu and Y. Zhou, Biophys. J. **100**, 2475 (2011).
[35] M. Born, Z. Phys. **1**, 45 (1920).
[36] V. Markin and A. Vollov, J. Electroanal. Chem. Interfacial Electrochem. **235**, 23 (1987).
[37] P. Atkins and J. de Paula, *Physical Chemistry*, 9th ed. (Oxford University Press, W. H. Freeman and Company, 2009).
[38] K. N. Piasta, D. L. Theobald, and C. Miller, J. Gen. Physiol. **138**, 421 (2011).
[39] B. Roux, S. Bernèche, B. Egwolf, B. Lev, S. Y. Noskov, C. N. Rowley, and H. Yu, J. Gen. Physiol. **137**, 415 (2011).
[40] S. Y. Noskov, S. Berneche, and B. Roux, Nature **431**, 830 (2004).
[41] W. Im and B. Roux, J. Mol. Biol. **322**, 851 (2002).
[42] S. Y. Noskov, W. Im, and B. Roux, Biophys. J. **87**, 2299 (2004).
[43] J.-L. Liu, D. Xie, and B. Eisenberg, Comput. Math. Biophys. **5**, 116 (2017).
[44] J.-L. Liu and B. Eisenberg, Phys. Rev. E **92**, 012711 (2015).
[45] B. Eisenberg, Y. Hyon, and C. Liu, J. Chem. Phys. **133**, 104104 (2010).
[46] B. Eisenberg, Y. Hyon, and C. Liu, Commun. Math. Sci. **9**, 459 (2011).
[47] D. Boda, W. Nonner, M. Valiskó, D. Henderson, B. Eisenberg, and D. Gillespie, Biophys. J. **93**, 1960 (2007).
[48] D. Boda, W. Nonner, D. Henderson, B. Eisenberg, and D. Gillespie, Biophys. J. **94**, 3486 (2008).
[49] D. Boda, M. Valiskó, D. Henderson, B. Eisenberg, D. Gillespie, and W. Nonner, J. Gen. Physiol. **133**, 497 (2009).
[50] B. Eisenberg and W. Liu, Comput. Math. Biophys. **5**, 125 (2017).
[51] I. Rubinstein, *Electro-Diffusion of Ions* (SIAM, Philadelphia, PA, 1990).
[52] W. Liu, Comput. Math. Biophys. **6**, 28 (2018).
[53] L. Zhang, B. Eisenberg, and W. Liu, Eur. Phys. J.: Spec. Top. **227**, 2575 (2019).
[54] W. Nonner, D. P. Chen, and B. Eisenberg, J. Gen. Physiol. **113**, 773 1999).
[55] U. Hollerbach, D. P. Chen, D. D. Busath, and B. Eisenberg, Langmuir **16**, 5509 (2000).
[56] M. S. Kilic, M. Z. Bazant, and A. Ajdari, Phys. Rev. E **75**, 021502 (2007).
[57] M. Burger, B. Schlake, and M.-T. Wolfram, Nonlinearity **25**, 961 (2012).
[58] B. Nadler, U. Hollerbach, and R. S. Eisenberg, Phys. Rev. E **68**, 021905 (2003).
[59] B. Egwolf and B. Roux, J. Mol. Biol. **401**, 831 (2010).
[60] V. B. Luzhkov and J. Åqvist, Biochim. Biophys. Acta (BBA)—Protein Struct. Mol. Enzymol. **1548**, 194 (2001).
[61] I. H. Shrivastava, D. P. Tieleman, P. C. Biggin, and M. S. Sansom, Biophys. J. **83**, 633 (2002).
[62] L. Heginbotham, M. LeMasurier, L. Kolmakova-Partensky, and C. Miller, J. Gen. Physiol. **114**, 551 (1999).
[63] M. LeMasurier, L. Heginbotham, and C. Miller, J. Gen. Physiol. **118**, 303 (2001).
[64] R. L. De Nó, J. Cell. Comp. Physiol. **33**, 3 (1949).
[65] P. Fatt and B. Ginsborg, J. Physiol. **142**, 516 (1958).
[66] C. N. Rowley and B. Roux, J. Gen. Physiol. **142**, 451 (2013).
[67] W. Im and B. Roux, J. Chem. Phys. **115**, 4850 (2001).
[68] S.-H. Chung and S. Kuyucak, Biochim. Biophys. Acta (BBA)—Biomembranes **1565**, 267 (2002).
[69] S. Furini, F. Zerbetto, and S. Cavalcanti, Biophys. J. **91**, 3162 (2006).
[70] S. Bernèche and B. Roux, Proc. Natl. Acad. Sci. USA **100**, 8644 (2003).
[71] Z. Song, X. Cao, and H. Huang, Phys. Rev. E **97**, 012411 (2018).
[72] R. Beals and R. Wong, *Special Functions and Orthogonal Polynomials*, Vol. 153 (Cambridge University Press, Cambridge, 2016).
[73] C. M. Nimigean and T. W. Allen, J. Gen. Physiol. **137**, 405 (2011).
[74] J. Malmivuo, R. Plonsey *et al.*, *Bioelectromagnetism: Principles and Applications of Bioelectric and Biomagnetic Fields* (Oxford University Press, New York, 1995).